Earth-Science Reviews 237 (2023) 104292

Contents lists available at ScienceDirect

Earth-Science Reviews

journal homepage: www.elsevier.com/locate/earscirev

Towards a kerogen-to-graphite kinetic model by means of Raman spectroscopy

A. Schito *, D.K. Muirhead, J. Parnell

Department of Geology and Geophysics, School of Geosciences, University of Aberdeen, Aberdeen AB24 3UE, UK

ARTICLE INFO

Keywords:
Carbonaceous material
Raman spectroscopy
Heating rate
Magmatic intrusions
Rock-Eval Pyrolysis
Frictional heating
Charcoals
Kinetics

ABSTRACT

Raman spectroscopy on carbonaceous material has become the most used geothermometer in Earth science studies. However, its application in very different settings, associated with different heating rates, demands an updated review to understand the different paths of maturation that can occur in the geological record. A comparison between organic matter matured under slow (diagenesis and regional metamorphism) or fast (around shallow intrusion or under artificial pyrolysis) heating rates highlight a mismatch between Raman spectra at the same thermal maturity. Such differences are probably due to the interplay of kinetics and strain, and highlights that classical kinetics based on vitrinite reflectance is not appropriated when Raman parameters are used. In the controversial application to faults and shear zones a review of existing literature indicates that a distinction is needed between strain and frictional heating effects since they lead to different spectra evolution. The effect of strain enhances organic matter aromaticity, while data from frictional heating experiments show strong analogies with charcoal spectra even if the kinetics of the process still need to be understood. All this evidence emphasizes that Raman spectroscopy is a powerful tool to describe the aromatization experienced by carbon material in most of the natural conditions and is a good candidate for the development of a universal geothermometer based on a new kinetic model for Earth and planetary sciences.

1. Introduction

Carbonaceous material (CM) dispersed in rocks derives mostly from the diagenetic alteration of the remains of organisms incorporated in sedimentary rocks during progressive burial. The residue left after the generation and expulsion of hydrocarbons (i.e., kerogen) becomes more enriched in carbon and rearranges into more condensed compounds, via the so-called aromatization process, progressing toward high temperatures. The increase of aromatization in CM is probably the most sensitive geological process to temperature variations and, therefore, has been widely applied as a geothermometer. Organic matter–based geothermometry is generally applied to studies focussed on the thermal state of the crust during diagenesis and metamorphism (Allen and Allen, 2013; Beyssac and Rumble, 2014) or to geologically fast heating (from here onwards called as 'transient heating') processes such as frictional heating on faults planes during earthquakes (Kitamura et al., 2012; Sheppard et al., 2015; Rabinowitz et al., 2020), wildfires (Marynowski and Simoneit, 2009), pyroclastic flows (Scott and Glasspool, 2005) and meteorite impact/atmospheric entry (Amari et al., 1990; Parnell et al., 2005, 2011). Notably, graphite can also form by precipitation from volcanic organic-rich hydrothermal fluids (Lindgren and Parnell, 2006) or by metamorphic fluids derived from mineral reactions (Rumble, 2014) including decarbonation in subduction zones (Galvez et al., 2013).

CM Geothermometry has utilized methods such as elemental analysis, Rock-Eval Pyrolysis and vitrinite reflectance since the middle of the last century. However, in the last thirty years Raman spectroscopy has become a promising tool for the analysis of CM since it provides great accuracy at the microscale, avoiding time-consuming preparation.

The volume of studies using Raman spectroscopy as a carbonaceous material (RSCM) geothermometer has greatly increased in the last decade (see Henry et al., 2019a for a complete review) and, consequently, a general correlation between Raman spectra evolution and diagenetic/metamorphic ranks has been deduced as shown in Fig. 1. Nevertheless, the application to diagenetic and metamorphic studies (Beyssac et al., 2002; Guedes et al., 2010; Lahfid et al., 2010; Liu et al., 2013; Lünsdorf et al., 2017; Wilkins et al., 2014; Schito et al., 2017; Henry et al., 2018; Corrado et al., 2020; Muirhead et al., 2020) still

* Corresponding author.
E-mail address: andrea.schito@abdn.ac.uk (A. Schito).

https://doi.org/10.1016/j.earscirev.2022.104292
Received 17 August 2022; Received in revised form 9 December 2022; Accepted 16 December 2022
Available online 20 December 2022

outnumbers alternative applications like maturation around shallow intrusions (Muirhead et al., 2012; Chen et al., 2017; Muirhead et al., 2017; Henry et al., 2019a, 2019b; Li et al., 2020), contact metamorphism at deeper levels (Aoya et al., 2010; Beyssac et al., 2019; Mori et al., 2017; Li et al., 2019), frictional heating on fault planes (Ito et al., 2017; Nakamura et al., 2015; Kedar et al., 2020; 2022; Muirhead et al., 2021) or charring temperatures of charcoal in natural wildfires (Theurer et al., 2021, 2022). In other words, the research has been mainly focused on the evolution of Raman data under low heating rates and is not clear how different heating (and pressure) conditions can affect it. Some studies point out a mismatch between Raman parameters and vitrinite reflectance evolution under natural and artificial maturation conditions (Hackley and Lünsdorf, 2018; Khatibi et al., 2019; Hao et al., 2019; Hackley et al., 2022; Sanders et al., 2022), but this has not been verified in natural settings or under extreme conditions such as frictional heating or wildfires (Kitamura et al., 2012; Hirono et al., 2015; Deldicque et al., 2016; Kaneki et al., 2016; Ito et al., 2017; Kaneki and Hirono, 2018; Theurer et al., 2021; Schito et al., 2022).

Diagenetic/metamorphic and frictional heating trends in Raman data have been already reviewed by Henry et al. (2019a), but in light of

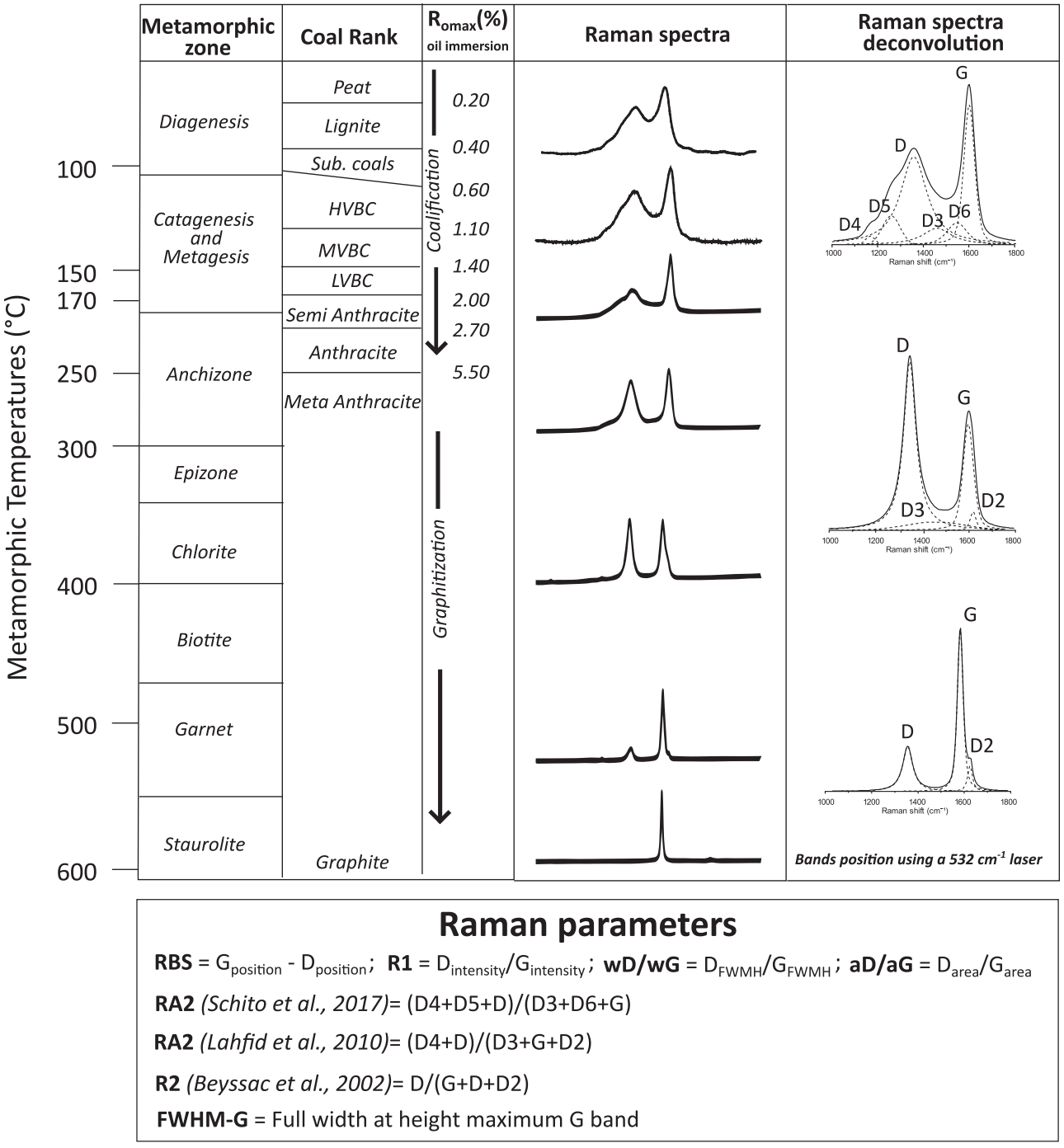

Fig. 1. Diagram showing metamorphic zones, coal ranks, vitrinite reflectance and corresponding Raman spectra. Correlation with metamorphic ranks and vitrinite reflectance is from Hunt (1995). Correlation of Raman spectra and deconvolution are after Schito et al., 2017, Lahfid et al., 2010 and Beyssac et al., 2002. Bands nomenclature is after Henry et al. (2019a). Abbreviations: Sub. Coals- subituminous coals; HVBC – high volatile bituminous coals; MVBC – medium volatile bituminous coals; LVBM – low volatiles bituminous coals: $R_{omax:}$ maximum vitrinite reflectance under oil immersion.

the exceptional publishing rate on this topic we saw the need of a further review, to compare: 1) the coalification and graphitization trends under different thermal conditions (i.e., diagenesis/regional metamorphism versus contact metamorphism or pyrolysis) and 2) the CM aromatization degree under transient heating conditions that can be found in nature (i.e., wildfire or frictional heating). The main aim of this work is to suggest how a Raman-based kinetic model for CM can be derived in the future, applicable for most natural heating conditions.

2. Raman spectrum and fitting approaches

The Raman spectrum of CM comprises the two main D (disorder) and G (graphite) bands and other minor bands in the so-called first-order region between 1000 and 2000 cm^{-1} (Fig. 1). Other bands in the second-order region between 2900 and 3200 cm^{-1} become visible only through graphitization. The G band is related to the E_{2g} symmetry in-plane vibration of carbon atoms in graphene sheets and is active in crystalline graphite at 1582 cm^{-1} (Tuinstra and Koenig, 1970; Reich and Thomsen, 2004; Pimenta et al., 2007). Two hypotheses on the origin of the D band at 1350 cm^{-1}, active in disordered graphite, relate it to a double resonant Raman scattering process (Pócsik et al., 1998; Reich and Thomsen, 2004; Pimenta et al., 2007), or alternatively to the ring-breathing vibration in the graphite subunit or polycyclic aromatic compounds (PAHs) (Negri et al., 2004; Castiglioni et al., 2004; Lünsdorf, 2016).

Two additional bands, at approximately 1620 and 1500 cm^{-1} (D2 and D6 in Fig. 1; Nemanich and Solin, 1979; Beny-Bassez and Rouzaud, 1984; Beyssac et al., 2002; Lünsdorf, 2016), are generally attributed to lattice-induced defects or to out-of-plane tetrahedral carbons, respectively. An additional band at about 1200 cm^{-1} (D5, Fig. 1) derives from sp^3–sp^2 bonds or C—C and C = C stretching vibrations of polyene-like structures (Sadezky et al., 2005; Lahfid et al., 2010). More bands have been related to C—H species in aliphatic hydrocarbon chains (Ferralis et al., 2016) or to polyacetylene-like structures (Rebelo et al., 2016) and mainly lie in the region between 1150 and 1250 cm^{-1} or at 1400 cm^{-1} (respectively D4 and D3 in Fig. 1).

The strong signal of these bands is due to the resonant effect between the aromatic compounds in CM and the wavelength of the most used excitation lasers (Ferrari and Robertson, 2000). This effect, however, implies that other non-resonant species appear at much lower intensities (up to 10^{-5}) and are totally overwhelmed by the resonant species (Marshall et al., 2010). Therefore, Raman technology on CM is mainly insensitive to aliphatic or oxygenated groups that other techniques, like Fourier Transform Infrared Spectroscopy (FT-IR) or Nuclear Magnetic Resonance (NMR), can detect.

The main changes in Raman spectrum in the low temperature zone (i.e., coalification) are related to the shift in the D band position (Lünsdorf, 2016; Schito et al., 2017) due to the conversion of the conjugated linear PAHs into more compact (i.e., circular) structures (Castiglioni et al., 2004). Also, the minor bands that lie between 1100 and 1300 cm^{-1} and between 1400 and 1500 cm^{-1} disappear, possibly because of a decrease of methyl groups in alkane chains (Ferralis et al., 2016; Hackley and Lünsdorf, 2018). In metamorphosed samples, the progressive disappearance of the D bands and the shift of G band toward its graphitic position at 1582 cm^{-1} define the path of graphitization (Beyssac et al., 2002).

Parameters determined after spectrum deconvolution have been used in early works to determine the metamorphic grade (Pasteris and Wopenka, 1991; Wopenka and Pasteris, 1993; Spötl et al., 1998) and finally formalized as RSCM geothermometer by Beyssac et al. (2002) in the paleo-temperatures range between 330 and 650 °C. The RCSM method was later extended to the lower temperatures of metamorphism by Lahfid et al. (2010) and Lünsdorf et al. (2017) and it is now widely used as a thermal maturity tool in diagenesis (Guedes et al., 2010; Liu et al., 2013; Wilkins et al., 2014; Schito et al., 2017; Schito and Corrado, 2020; Henry et al., 2019a, Muirhead et al., 2020). The most recent review, compiled by Henry et al. (2019a), demonstrates that the Raman parameters that better correlate against thermal maturity and/or metamorphic paleo-temperatures are: distance between the D and the G bands (Raman Band Separation - RBS); the full width at maximum height of the G band (FWMH-G); the ratios of the D and G bands full width at maximum height (FWMH-D/FWMH-G), area (aD/aG) and peak intensities (R1). Parameters derived from the area ratio between the bands beneath the region around the D and the G bands are also generally used (RA2, R2, Fig. 1) in metamorphism (Beyssac et al., 2002: Lahfid et al., 2010) and in diagenesis (Schito et al., 2017).

Different fitting approaches can lead to misleading interpretation when they are based on a single parameter (e.g., RBS, R1, etc.). Thus, for the purpose of this work, spectra will be shown together with trend parameters. Spectra have been redrawn from published works and normalized with respect to the height of the G band.

3. Methods and heating regimes

Carbon is preserved in the geological record in its reduced form as the product of diagenetic and metamorphic transformations during burial (i.e., kerogen and graphite), charring (charcoals) and hydrothermal precipitation. Excluding the latter, the kinetics of such transformations is mainly driven by temperature and time while pressure starts to affect only above the diagenesis - low metamorphism boundary. The evolution of temperature through time varies according to different geological processes. It can be constant for million years during diagenesis and regional metamorphism, or for hundreds or a few thousands of years around an intrusion in the shallow crust. On the other hand, there are a variety of processes in which heating can be considered as instantaneous (from a geological point of view), lasting from days in the case of wildfires (Theurer et al., 2021) up to few seconds during seismic frictional heating (Kuo et al., 2017) on fault planes or due to the thermal shock of meteorite impact (Brolly et al., 2017).

3.1. Intrusion

When assessing maturation due to an igneous intrusion, a distinction between shallow and deep intrusions is required. The first case includes immature or early mature shales (Muirhead et al., 2012; Henry et al., 2019b) and coals (Chen et al., 2017; Henry et al., 2019b; Li et al., 2020) intruded by small (<10 m) mafic dike or sills at relatively shallow depths (generally <2 km). Deep intrusions such as granitic plutons of several km size (Aoya et al., 2010; Beyssac et al., 2019; Li et al., 2019; Yuan et al., 2021; Zhang et al., 2021) at relatively high pressures (at least 2–3 kbar) favour the graphitization process. Temperatures around intrusions can be calculated by numerical models (Galushkin, 1997; Aarnes et al., 2011; Muirhead et al., 2012; Wang, 2012; Iyer et al., 2013, 2017; Mori et al., 2017) or, in some cases, from vitrinite reflectance (Ro%) conversion (Li et al., 2020).

The characteristics of intrusions, host rocks, range of Ro% and temperatures and fitting approach for Raman spectra used by different authors are summarized in Table 1.

3.2. Artificial maturation

Artificial maturation experiments can be classified on the basis of pyrolysis approaches used by the authors (summarized in Table 2).

Kelemen and Fang (2001) first provided both isothermal and non-isothermal artificial pyrolysis experiments using an ultrahigh vacuum on a type I and II kerogen.

Hackley and Lünsdorf (2018) and Khatibi et al. (2019) explored the low-maturity stages of solid bitumen, heating their samples with hydrous pyrolysis (HP) according to the method of Lewan (1983) in a temperature range between 300 and 360 °C, where the maximum temperatures were kept for 72 h and the pressure was lower than 20 MPa. The same system was used by Birdwell et al. (2021), Hackley et al. (2022) and Sanders et al. (2022).

Table 1
Intrusions' and host rocks' properties together with Ro% and temperature ranges and fitting approach used by different authors dealing with CM Raman evolution around intrusions. n.d. – not determined. Ro% and T (°C) ranges include minimum and maximum.

Authors	Intrusion	Intrusion thickness (m)	Maximum distance from the intrusion (m)	Lithologies	Ro% range	Temperature range (°C)	Methods to calculate T (°C)	Fitting approach (n of bands)	Laser (cm^{-1})
Li et al., *2020*	n.d.	n.d.	8	Coal	0.55–5.0	76–358	Conversion from Ro by means of Barker and Pawlewicz (1994)	2	532
Chen et al., *2017*	Gabbroid dyke	3	6	Coal	0.85–3.01	122–490	Conversion from Ro by means of Bostick and Pawlewicz, 1984)	5	514.5
Henry et al., *2019b*	Dolerite	n.d.	n.d.	Coals and shales	0.47–6.04	n.d.	n.d.	no deconvolution	514.5
Zhang et al., *2021*	Granite	n.d.	150–1000	Coal	1.67–6.62	n.d.	n.d.	3/4	532
Li et al., *2019*	Granite	n.d.	300–21*10^3	Coal	3.63–8.23	n.d.	n.d.	4	532
Yuan et al., *2021*	Granite	n.d.	n.d.	Coal	3.11–7.69	n.d.	n.d.	3/4	532
Mori et al., *2017*	Dolerite	20–80	5–113	Mudstones and shales	n.d.	300–751	Numerical modelling	4	532
Aoya et al., *2010*	Granite	n.d.	n.d.	Metapelites	n.d.	340–665	Numerical modelling and petrographic constraints	4	532
Beyssac et al., *2019*	Granite	n.d.	n.d.	Metapelites	n.d.	495–645	Petrography	3/4	514.5

Table 2
Experimental condition and organic matter type (including single macerals when specified) for artificial pyrolysis experiments. *For IFORS method see Lünsdorf and Lünsdorf (2016). **Zhou et al. (2014) do not refer to number of bands but simply refer to Beyssac et al. (2003) that use 4 to 2 bands depending on the coal rank. In Ro %/BRo%/Rg% range column bitumen reflectance values (Bro%) are italicised and graptolite reflectance (Rg%) underlined.

Authors	Pyrolysis approach	Organi matter types	Fitting approach (n of bands)	Laser (cm^{-1})	Ro%/*BRo%*/Rg% range	T (°C) range	Time (hours)	Pressure (Mpa)
Hackley and Lünsdorf *(2018)*	Hydrous Pyrolysis	Solid bitumen	IFORS*	488	*0.39–1.28*	300–360	72	> 20
Khatibi et al. *(2019)*	Hydrous Pyrolysis	Solid bitumen	5	532	*0.38–0.92*	300–340	72	> 20
Hackley et al., *2022*	Hydrous Pyrolysis	Solid bitumen	3	532	*0.33–1.57*	300–370	72	> 20
Sanders et al., *2022*	Hydrous Pyrolysis	Artificial Samples (vitrinite-rich)/ Solid bitumen	3/4	473	0.77–0.97/ *0.24–0.54*	300–360	72	> 20
Birdwell et al., *2021*	Hydrous Pyrolysis	AOM/Liptodetrinite/ Vitrinite/ Solid bitumen	4	473	*0.13–0.77*	300–330	72	> 20
Du et al., *2014*	Semi-open pyrolysis	Type II kerogen	n.d.	532	0.49–3.60	280–560	72	80
	Golden tube closed system	Type II kerogen	n.d.	532	0.39–1.65	280–480	72	45
	Glass tube closed system	Type II kerogen	n.d.	532	1.61–2.71	320–500	72	45
Mi et al., *2019*	Golden tube closed system	Type I kerogen	No deconvolution	532	0.55–5.32	300–600	n.d.	n.d.
	Golden tube closed system	Type II kerogen	No deconvolution	532	0.55–5.32	300–600	n.d.	n.d.
	Golden tube closed system	Type III kerogen	No deconvolution	532	0.55–5.32	300–600	n.d.	n.d.
Zhou et al., *2014*	Golden tube closed system	Solid Bitumen	2/4**	532	*0.65–4.81*	300–750	n.d.	n.d.
Hao et al., *2019*	Closed system	Graptolites	4	532	0.62–3.07	350–550	72	100
	Closed system	Graptolites	4	532	3.55–4.03	550	432	50
Kelemen and Fang, *2001*	Ultrahigh Vacuum	Type I kerogen	2	632	0.68–3.37	200–690	n.d.	n.d.
	Ultrahigh Vacuum	Type II kerogen	2	632	0.68–3.37	200–690	n.d.	n.d.
Bonoldi et al., *2016*	Open-hydrous Pyrolysis	Type I kerogen	6	532	0.54–1.84	<360	n.d.	30
	Open-hydrous Pyrolysis	Type II kerogen	6	532	0.22–1.90	<360	n.d.	30

Bonoldi et al. (2016) use an open-hydrous system to maturate type I, II and III kerogen samples to temperatures up to 360 °C under a pressure of 30 MPa.

Du et al. (2014) compare parameters from three different pyrolysis methods: semi-open pyrolysis, and closed systems with a gold tube or glass tube. In the semi-open system, volatile pyrolyzates derived from primary cracking are removed from the reaction system at each pyrolysis step and then organic material is re-heated (Takahashi and Suzuki, 2017). Samples for semi-open pyrolysis are muddy source rocks representing a type II kerogen heated between 280 and 560 °C for 72 h under a constant pressure of 80 MPa. In the closed system, the authors study isolated kerogen in a temperature interval between 280 and 480 °C for 72 h under a constant pressure of 45 MPa using a gold tube, while closed glass tube system experiments are performed between 320 and 500 °C for 72 h under a constant pressure of 45 MPa.

Mi et al. (2019) and Zhou et al. (2014) work on artificially matured samples between about 300 °C up to 600 °C and 750 °C respectively, in a closed gold tube system. Mi et al. (2019) analysed coals and oil-shales that represent the main kinds of kerogen (i.e., types I, II and III), while Zhou et al. (2014) tested artificial pyrolysis on bitumen samples.

Hao et al., 2019 artificially mature graptolite-rich samples from the Ordovician Alum shales (Estonia) and Wufeng-Longmaxi Formation (China). Their samples are heated in a closed system at temperatures of 350, 400, 450 and 500 °C for 72 h and of 550 °C for 72, 288 and 432 h, keeping a lithostatic and a hydrostatic pressure of 100 MPa and 50 MPa respectively.

All experimental settings are summarized in Table 2.

3.3. CM maturation due to frictional heating or strain effects

Many authors have tried to quantify the frictional heating on a fault plane (Hirono et al., 2015; Ito et al., 2017; Kouketsu et al., 2017; Kuo et al., 2018a, 2018b; Nakamura et al., 2015) or the effect of the additional strain in aseismic shear zones on CM ordering (Kedar et al., 2020, 2021; Muirhead et al., 2021). In both cases, similar approaches were utilized, analysing samples in the less deformed host rocks, moving progressively toward subzones of increasing deformation (e.g., damage zone, breccia zone and gouge zone). Samples' preparation include thin sections, concentrated CM and clay-size residue deposited on glass slides. Some authors perform artificial maturation experiment for comparison with natural cases. Experiments include pure (isothermal) friction, transient heating experiments or the application of both (Kaneki et al., 2018). Pure friction experiments (Furuichi et al., 2015; Hirono et al., 2015; Kuo et al., 2017; Kirilova et al., 2018; Fan et al., 2020) are performed using a rotary shear apparatus under room temperature conditions, and normal stresses that vary between 1 and 3 MPa (Hirono et al., 2015; Kaneki et al., 2018), 2.7 and 13 MPa (Ito et al., 2017; Kuo et al., 2017) or 20–60 MPa (Fan et al., 2020) (Table 3).

Those authors who aim to reproduce the heating (Table 3) induced on the fault slip plane during earthquakes use a combination of heating rates (10 °C/min up to 100 °C/s). Even if the authors are aware that the typical heating rate on a slip plane can be tens to hundreds of °C per seconds (Kaneki et al., 2016), most of the experiments are performed between 10 and 50 °C/min (Hirono et al., 2015; Kaneki et al., 2018; Kaneki and Hirono, 2018) and only Kaneki and Hirono (2018) perform experiments at a maximum of 100 °C/s. At the same conditions, Ito et al. (2017) were able to artificially reproduce pseudotachylytes under high normal stresses, reaching temperatures between 850 and 1100 °C (as

Table 3
Experimental conditions for frictional and transient heating.

				Frictional heating						
Authors	Charring methods	Starting materials	Fitting approach (n of bands)	Laser (cm^{-1})	T (°C) range	Time (hours)	Heating rates (°C/min)	Normal Stresses (Mpa)	Velocity (ms^{-1})	Displacement (m)
Hirono et al., *2015*	Rotary shear	Kerogen	2	532	room T	n.d.	n.d.	1	0.01 to 1	5 to 16
Furuichi et al., 2015	Rotary shear	Low grade brown coal	6	532	room T to 500	9 s	n.d.	2	1.3	11
Ito et al., *2017*	Rotary shear	Low grade metamorphic CM	4	514.5	room T to 1100	4–16 s	n.d.	2.7–13.3	1.1	5.4–17.8
Kirilova et al., *2018*	Brittle Rock deformation Versatile Apparatus (BRAVA)	Graphite	3	532	n.d.	n.d.	n.d.	5 to 25	0.001–0.1	0.05–0.02
Kaneki et al., *2018*	Rotary shear	Kerogen	2	532	32.5	n.d.	n.d.	1 to 3	0.001	10
Fan et al., *2020*	Rotary shear	Bituminous Coal	No deconvolution	514.5	100	n.d.	n.d.	25–45	0.0001–0.1	0.0057
				Transient heating						
Hirono et al., 2015	TG-Calorimenter under air or argon atmosphere	Kerogen	2	532	100–900	n.d.	20	–	–	–
Kaneki et al., *2016*	TG-Calorimenter under air or argon atmosphere	Kerogen	2	532	100–1000	1 m	50	–	–	–
Mukoyoshi et al., 2018	Thermogravimetric apparatus in Ar atmosphere	Kerogen	2	532	100–1300	n.d.	50	–	–	–
Kaneki et al., 2018	TG-Calorimenter under air or argon atmosphere	Kerogen	4	532	100–1000	n.d.	50	–	–	–
	Tube furnace				1100–1300		15	–	–	–
Kaneki and Hirono, 2018	TG-Calorimenter under air or argon atmosphere	Kerogen	2	532	50–1000	n.d.	50	–	–	–
	Tube furnace				100–1000	10 s	500	–	–	–

determined by the evidence of illite dehydration and decomposition), while Kuo et al. (2014, 2017) demonstrate, by high slipe rate experiments, that high temperature along slip zone could facilitate the formation of graphite whose presence can be consider as a seismic indicator. Notably, in rotary shear experiments, temperatures have been always measured by means of thermocouple. However, this method can have large uncertainty as outlined by a recent work from Aretusini et al. (2021) that show the use of optical fibres significantly improve the accuracy. Unfortunately, such technology has not been yet used in experimental sheared CM.

The relatively low heating rate experiments are performed using a calorimeter apparatus under Ar gas flow in order to remove the products of pyrolysis (i.e., semi-open system), while for fast heating experiment a tube furnace is used under vacuum condition to replicate anoxic condition of faults at depth.

The starting material for such experiments includes immature kerogen (Mukoyoshi et al., 2018), late diagenetic kerogen (Hirono et al., 2015; Kaneki et al., 2016; Kaneki and Hirono, 2018), low metamorphosed organic matter (Ito et al., 2017) and an artificial mixture of 90% of quartz and 10% of lignite corresponding to an immature wood-derived kerogen (Kaneki et al., 2018).

3.4. Natural and artificial charring

Raman spectroscopy on wood-derived charcoals has been used to assess charring temperatures with implications in paleo-wildfires for paleoecological and volcanological studies (Ascough et al., 2010; Mauquoy et al., 2020; Theurer et al., 2021, 2022; Schito et al., 2022), or to evaluate coal and wood reactivity for metallurgical application (Urban et al., 2003; Paris et al., 2005; Zickler et al., 2006; Chabalala et al., 2011; Morga, 2011; Surup et al., 2019) (Table 4). Studies dealing with other fuel types (i.e., biomass char) or on the effect of catalysts on char reactivity at very high temperatures (from 1500 to 2700 °C) are not considered.

Some authors compare experimentally heated samples with natural wildfire, finding a good agreement between natural and artificial charcoals (Yamauchi and Kurimoto, 2003; Paris et al., 2005; Zickler et al., 2006; Ishimaru et al., 2007; Deldicque et al., 2016; Surup et al., 2019; Theurer et al., 2021), while Urban et al. (2003), Chabalala et al. (2011) and Morga (2011) show the evolution of experimentally charred coals.

Charcoalification experiments mainly consist of charring into a furnace or electric oven under nitrogen atmosphere at heating rates varying between 0.5–5C°/min (Urban et al., 2003; Paris et al., 2005; Zickler et al., 2006; Theurer et al., 2021), 10–15 °C/min (Surup et al., 2019; Ishimaru et al., 2007; Chabalala et al., 2011) or 20–60 °C/min (Yamauchi and Kurimoto, 2003; Morga, 2011). Maximum temperatures are generally kept constant for 0.5 to 12 h. Most of the authors work in a temperature range between 500 and 1200 °C·In detail, Yamauchi and Kurimoto (2003), Paris et al. (2005), Chabalala et al. (2011) and Theurer et al. (2021) explore temperatures below 500 °C while only Urban et al. (2003), Zickler et al., 2006 and Chabalala et al. (2011) test higher temperatures up to 2500 °C on coal tar pitch or coals.

Morga (2011) perform high-temperature heating experiments to investigate the reactivity of coals rich in semifusinite and fusinite. These macerals, similarly to vitrinite, derived from continental plant with the difference that they suffered oxidation due to alteration in the atmosphere (dehydration and weathering), burning, fungal and bacterial decomposition (among others, see Coal I.C., 2001) before to be embedded in the sediments.

Samples from Schito et al. (2022) derive from charred plant material entombed in pyroclastic sediments and the maximum temperatures experienced are calculated from charcoal reflectance (Scott and Glasspool, 2005; Pensa et al., 2018) or from partial thermal remanent magnetization (pTRM; Pensa et al., 2015).

4. Raman trends against thermal maturity and temperatures

4.1. Artificial maturation and Intrusions

4.1.1. Comparing natural and artificial maturation

The main issue with artificial maturation is to verify if Raman spectra show the same characteristics with naturally matured samples at the same thermal maturity. This question has been addressed by Kelemen and Fang (2001), Hackley and Lünsdorf (2018), Khatibi et al. (2019), Bonoldi et al. (2016), Zhou et al. (2014) and Hao et al. (2019).

RBS is the most used parameter (Fig. 2a), while the FWHM-G was presented only in one study and was thus discarded in Fig. 2. Kelemen and Fang (2001), Zhou et al. (2014), Hackley and Lünsdorf (2018) and

Table 4
Experimental conditions for wood charring. *Schito et al., 2022 worked on natural samples charred by pyroclastic flows.

Authors	Charring methods	Starting materials	Fitting approach (n of bands)	Laser (cm^{-1})	T (°C) range	Time (hours)	Heating rates (°C/min)
Paris et al., *2005*)	Furnace under nitrogen atmosphere	Softwood (spruce and pine)	2	514.5	25–1400	2	2
Yamauchi and Kurimoto *(2003)*	Electric hoven under nitrogen atmosphere	Cedar wood (xylem and bark)	2/4	632.8	200–1100	3	20–27
Ishimaru et al., *2007*	Furnace under nitrogen atmosphere	Cedar wood	5	514.5	500–1000	1	4
Surup et al., *2019*	High-temperature Furnace	Spruce and oak wood	9	514	1200–1600	2	10
	Slow Pyrolysis reactor under nitrogen atmosphere				800–1200	0.5	
Deldicque et al., *2016*	Furnace under argon flow	Pinewood	No deconvolution	514.5	500–1200	1–6	n.d.
Theurer et al., *2021*	Furnace	Stems, roots and flowers	2	514.5	250–800	1.5	5
Schito et al., *2022*	*Pyroclastic flow	Pinewood	2	532	245–566	n.d.	n.d.
Zickler et al., *2006*	Furnace under nitrogen atmosphere	Spruce wood	2/5	532	400–2400	2	2–5
Urban et al., *2003*	HTT	Coal tar pitch	4	514.5	500–2500	5	0.5–4
Morga, 2011	Furnace under argon atmosphere	Semifusinite and fusinite in coals	5	514	400–1200	1	60
Chabalala et al., *2011*	Furnace under nitrogen atmosphere	Coals	3/4	532	300–1000	1	15
Sheng, 2007	Furnace under nitrogen atmosphere	Coals	5	514.5	1200–1800	n.d.	10

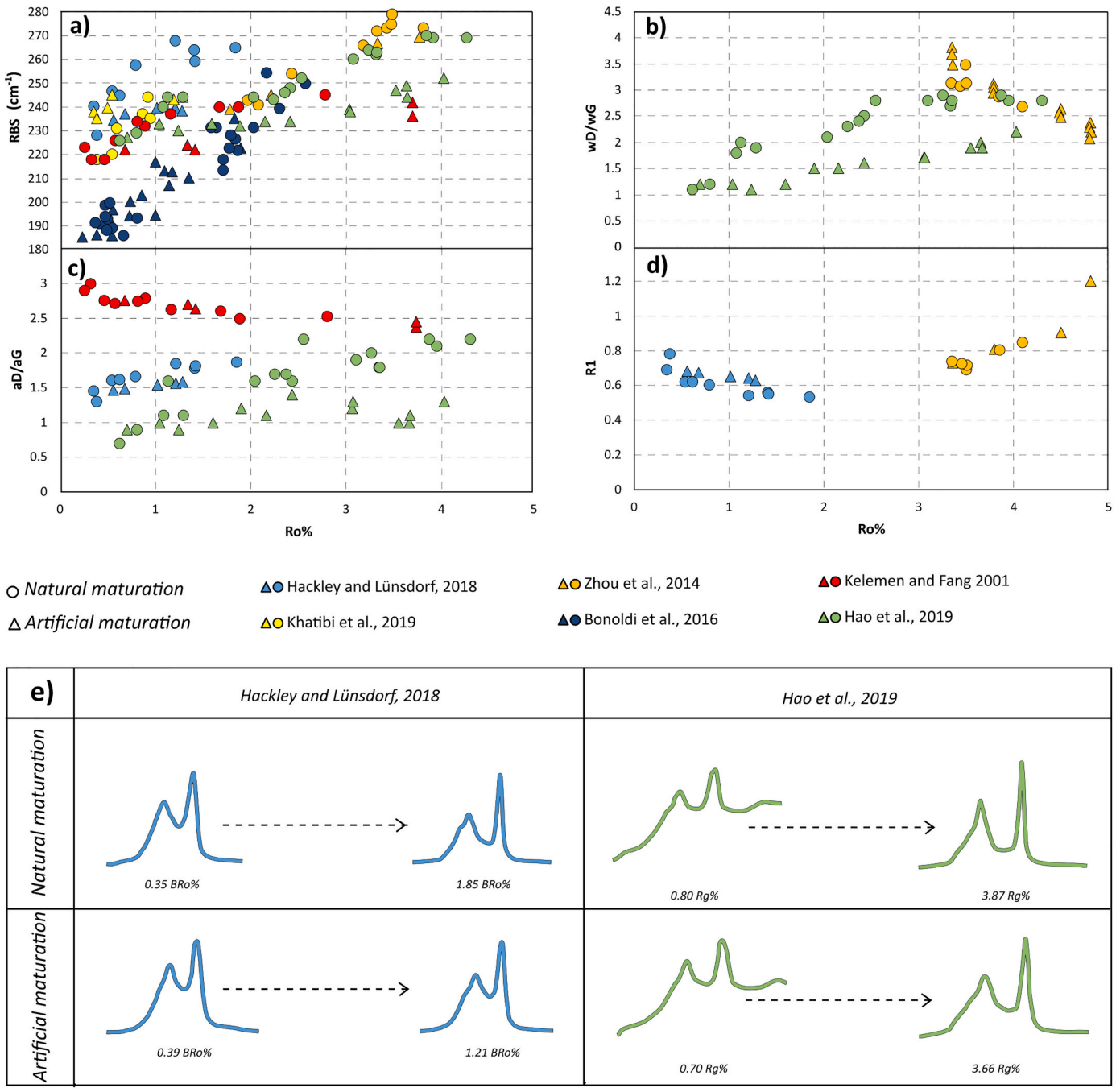

Fig. 2. Natural vs artificial maturation comparison by means of a) RBS; b) wD/wG; c) aD/aG and d) R1 parameters. Fig. e) shows spectra evolution in experiments from Hackley and Lünsdorf (2018) and Hao et al. (2019). In Figs. a-d Zhou et al. (2014), Hackley and Lünsdorf (2018) and Khatibi et al. (2019) measured reflectance on solid bitumen while Hao et al. (2019) on graptolites. In Hackley and Lünsdorf (2018) spectra are shown after baseline subtraction, while in Hao et al. (2019) low maturity spectra are characterized by strong fluorescence background. Acronyms: Ro%- vitrinite reflectance; BRo% - solid bitumen reflectance; Rg% - graptolite reflectance.

Hao et al. (2019) compare the width and intensity ratios (Fig. 2 b,d), while Kelemen and Fang (2001), Hackley and Lünsdorf (2018) and Hao et al. (2019) use the area ratio of the D and G bands (aD/aG parameter) that is introduced in Fig. 2c. The first works that compare natural and artificial maturation in kerogen and solid bitumen (Kelemen and Fang, 2001; Zhou et al., 2014; Bonoldi et al., 2016) claim no systematic differences (Fig. 2 a,b,d; Zhou et al., 2014; Bonoldi et al., 2016) exists or, alternatively, that differences can be detected by the RBS parameters but not by the others (Fig. 2b,c; Kelemen and Fang, 2001).

The works of Hackley and Lünsdorf (2018), Hao et al. (2019) and Khatibi et al. (2019) specifically address the issue of comparison. On the basis of HP experiments, both Hackley and Lünsdorf (2018) and Khatibi et al. (2019) state that Raman spectra of artificially matured solid bitumen systematically differ from spectra from natural examples. At higher maturities, such behaviour has been further confirmed by Hao et al. (2019); Figs.2a,b,c) working on graptolites. Their data outline a retardation of maturation for artificially matured samples as shown by spectra in Figs. 2e.

4.1.2. *Trends against Ro%*

Artificial pyrolysis reproduces geologically fast heating at relatively low lithostatic pressure (i.e., low burial) resembling conditions that can

be found during source rocks maturation around shallow intrusions, so data were reviewed together in Fig. 3.

As already stressed by Henry et al. (2019a), Raman parameter trends are strongly influenced by fitting approach, laser wavelength and starting material, so that only general trends can be depicted. In detail, the use of different laser wavelengths is known to affect the position of the D band (Quirico et al., 2005; Lünsdorf, 2016) and, consequently, the RBS value. Looking at Tables 1 and 2 and at Henry et al. (2019a) the green (514 to 533 cm^{-1})laser is the most used in literature. Assuming negligible differences between 514 cm^{-1} and 533 cm^{-1} lasers, however,

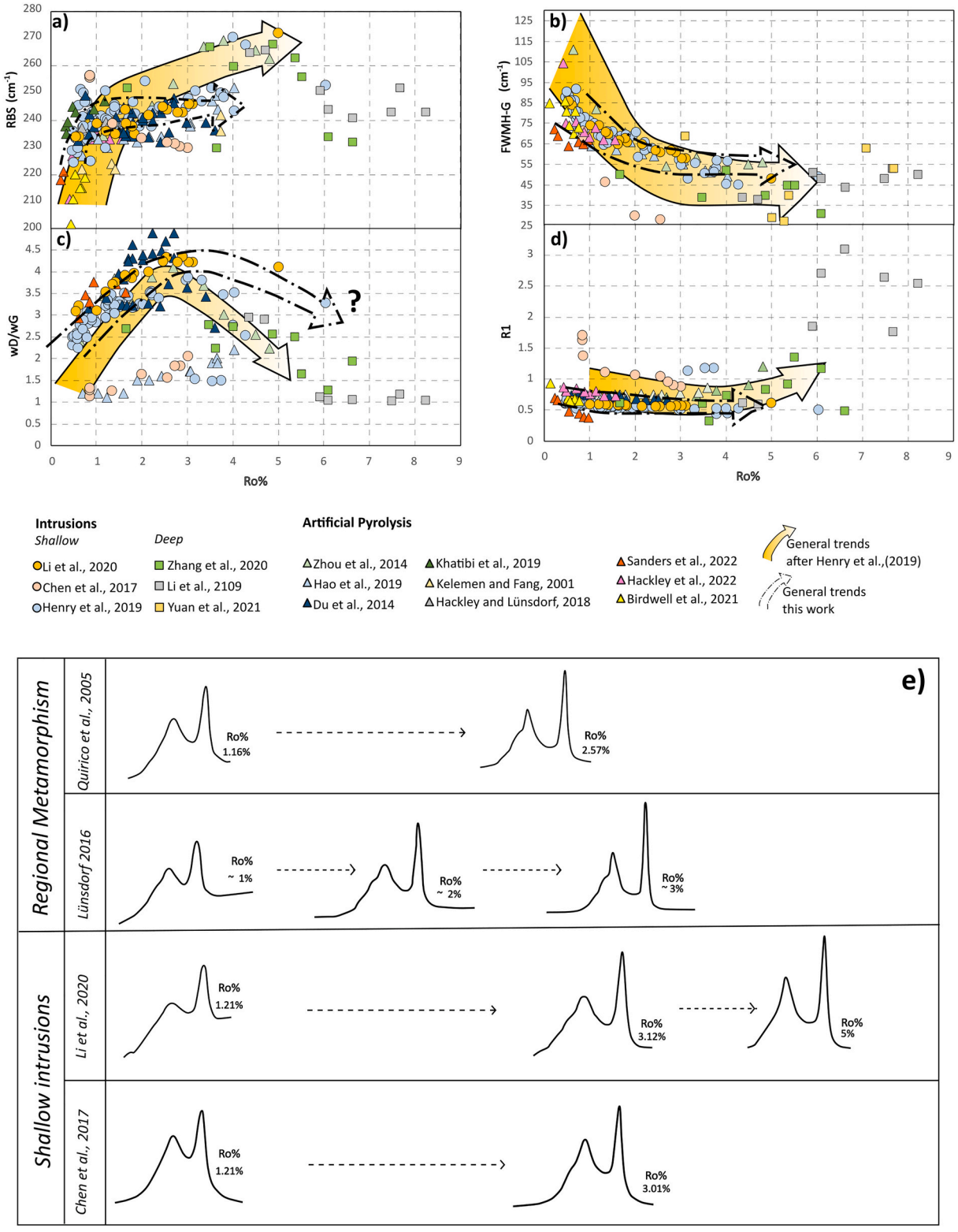

Fig. 3. Comparison of Raman parameters against reflectance measured on solid bitumen by Hackley and Lünsdorf (2018), Khatibi et al. (2019), Birdwell et al. (2021) and Hackley et al. (2022), on solid bitumen and vitrinite by Sanders et al. (2022), on graptolite by Hao et al. (2019) and on vitrinite by other authors.a) RBS; b) FWHM-G; c) wD/wG and d) R1 values. Orange arrows indicate general trends for diagenesis/regional metamorphism found by Henry et al. (2019a), while dotted arrows the ones from the present work. e) Redrawn spectra from Li et al. (2020); Lünsdorf (2016); Quirico et al. (2005) and Chen et al. (2017).

in Fig. 3, samples from Hackley and Lünsdorf (2018), Sanders et al. (2022), Birdwell et al. (2021) and Kelemen and Fang (2001) should be considered with caution since the authors use a 488 cm^{-1}, 473 cm^{-1} and 632 cm^{-1} lasers respectively. This implies that, taking as a reference measures made by a green laser, RBS is slightly underestimate for Hackley and Lünsdorf (2018), Sanders et al. (2022) and Birdwell et al. (2021) and overestimate in Kelemen and Fang (2001). As well, it should be considered that many works dealt with solid bitumen, whose reflectance (BRo% in Table 2), is usually lower than Ro% at the same thermal maturity. For these samples a slight shift toward higher values on the x-axis should be considered. The response of different macerals to heat-induced aromatization measured by Raman has been issued only by Birdwell et al. (2021). Analysing AOM, solid bitumen, liptodetrinite and vitrinite from the same samples, the authors conclude that different macerals progress along similar trend but can respond to a greater or lesser degree to the same level of thermal energy. From their preliminary data, solid bitumen seems to react faster to heating then vitrinite and AOM but more data are still needed to confirm this conclusion.

In Fig. 3, artificial pyrolysis and samples matured around shallow intrusions have been plotted together and compared with trends already depicted by Henry et al. (2019a) for samples matured in diagenesis and under regional metamorphism. New trends found in this work are marked with dotted arrows while Henry et al.'s (2019a) trends with orange-shaded arrows.

RBS values (Fig. 3a), for artificial maturation and shallow intrusions (triangles and circles) show an increase between about 0.4 to 4.0% Ro that seems to slow down after 2% Ro (Fig. 3a). This trend outlines a net mismatch with respect to the general trend detected by Henry et al., (2019a) for regional metamorphism (see arrows in Fig. 3a). At the highest maturities, the decrease of RBS values after 5% Ro marks the onset of the graphitization process for deeper intrusion samples (squares in Fig. 3a).

Triangles and circles in Fig. 3b mark a constant decrease of FWHM-G values during coalification at high heating rates (dotted arrow) but without the net decrease observed in regional metamorphism as marked by the change in slope of the coloured arrow between 2 and 3-Ro%. The mismatch is further evidenced by the lower values of deep intrusions samples (squares) between about 4 and 6 Ro% (Fig. 3b).

The wD/wG parameter shows an up and down trend with a turning point between 2 and 3% Ro and stable values after about 6% Ro (Fig. 3c). Even if they are not so easily interpreted (question mark in Fig. 3c), the main differences with the Henry et al. (2019a) trend are probably that, in values from shallow intrusions from Li et al. (2020) and Henry et al. (2019b) (orange and light blue circles, Fig. 3c), the turning point seems to be slightly shifted toward higher maturities and that artificially matured graptolitic shales from Hao et al. (2019) (light blue triangles) never decrease up to >4%.

Finally, no significant trends can be depicted for the R1 parameter (Fig. 3d) where values do not significantly change and lie at the lower limit of the orange arrow. An increase of R1 values at the onset of graphitization after 5% Ro was only detected for deep intrusion samples.

The mismatches outlined by the dotted and the yellow lines in Fig. 3 indicates a retarded aromatization trend for intrusion and artificial samples with respect to those matured under regional metamorphism. This is further highlighted by spectra in Figs. 3 e and f.

The mismatch, in particular between shallow intrusions and regional metamorphism/deeper intrusions, suggest differences can be mainly found at the highest thermal maturities. However, data for artificially matured samples in Hackley and Lünsdorf (2018), Khatibi et al. (2019) and Hao et al. (2019) in Fig. 2 show that Raman parameters can start to behave differently also at low thermal maturities, perhaps in the material studied by these authors (i.e. solid bitumen and graptolites). This suggests a kinetic effect on Raman spectra evolution, different from the one governing reflectance increase.

It should be noted that source rocks matured around intrusions experience different heating regimes according to their distance to the magmatic source. According to numerical simulations (Galushkin, 1997; Muirhead et al., 2012; Wang, 2012; Iyer et al., 2018) very high (up to 600 °C) maximum temperatures near the intrusion are maintained for a few months or years, while, at a distance equivalent to the intrusion thickness, they are kept for several hundreds of years. This implies that samples far from the intrusion probably experienced heating rates more similar to diagenetic conditions and that is likely why they better fit with the general trends of Fig. 3.

It should also be considered that in sedimentary basins, reflectance values higher than 3.5% (Fig. 3) generally correspond to very high burial depths where tectonic stress (i.e., pressure) can influence metamorphism of organic matter (Suchy et al., 1997; Barzoi, 2015). It is thus possible that the interplay of heating rate and pressure conditions could be the cause of the mismatch between the two trends.

In general, vitrinite reflectance and Raman parameters are related but they don't measure the same things. Reflectance is known to increase as a function of the refractive and absorption indexes that are related on the amount of delocalized electrons (Van Krevelen and Te Nijenhuis, 2009), while Raman spectrum directly give information on the aromaticity of the material. Carr and Williamson (1990) already show that a non-linear correlation between reflectance and aromaticity (measured by means of NMR) exist in kerogen, because the two methods respond differently to structural changes occurring during maturation in diagenesis and low metamorphism. Different rates were particularly observed for Ro% higher than 3% where the growth of aromatic sheets increase reflectance anisotropy (Carr and Williamson, 1990).

Results from the present review, suggest that under high heating rates and low tectonic stress the rate of aromaticity increase detected by Raman is lower than that under low metamorphic condition at the same vitrinite reflectance (i.e., thermal maturity).

Moreover, to understand the decoupling at lowest maturities, Hackley and Lünsdorf (2018) proposed that the retardation could be attributed to a greater abundance of methyl-substituted aliphatic hydrocarbons that probably hamper the growth of aromatic clusters in pyrolyzed samples.

Whatever the cause, data shown in Figs. 2 and 3, indicate that samples with the same Ro% values, but matured under different conditions, have different Raman spectra. This confirm that the molecular changes that drive Ro% increase are not the same and suggest their correlation vary according to different heating conditions.

4.1.3. *Trends against Temperature*

New trends found in Fig. 3 against Ro% can be also converted into paleotemperatures (Fig. 4) assuming the shift from Raman "geothermometer" to a "thermal maturity indicator" when moving from regional metamorphism toward shallow intrusions or artificial maturation. Regarding shallow intrusions, this issue has been faced only by few authors (Chen et al., 2017; Mori et al., 2017; Li et al., 2020) with still some problems, as outlined below.

Paleotemperatures around intrusions can be calculated by using different approaches. For studies on deep plutons, a thermal model calibrated by means of mineral assemblage in the host rock is probably the best approach (Aoya et al., 2010; Hilchie and Jamieson, 2014). In shaly formations, or in coals around shallow intrusions, reflectance measurements are mainly used. In general, few attempts (Chen et al., 2017; Li et al., 2020) have been reported in the literature to provide a correlation between Raman parameters and temperatures around shallow intrusions, and they both use empirical correlations to convert Ro% values into temperatures. Li et al. (2020) converted their data by means of the equation of Barker and Pawlewicz (1994), obtaining values between 80 and 350 °C, while the reflectance values of Chen et al. (2017) are converted by means of the Bostick and Pawlewicz (1984) equation and range between about 130 and 500 °C.

However, it is advisable to use Ro% data to calibrate a thermal model, rather than directly converting them into temperature by means of empirical equations (Galushkin, 1997; Aarnes et al., 2011; Muirhead

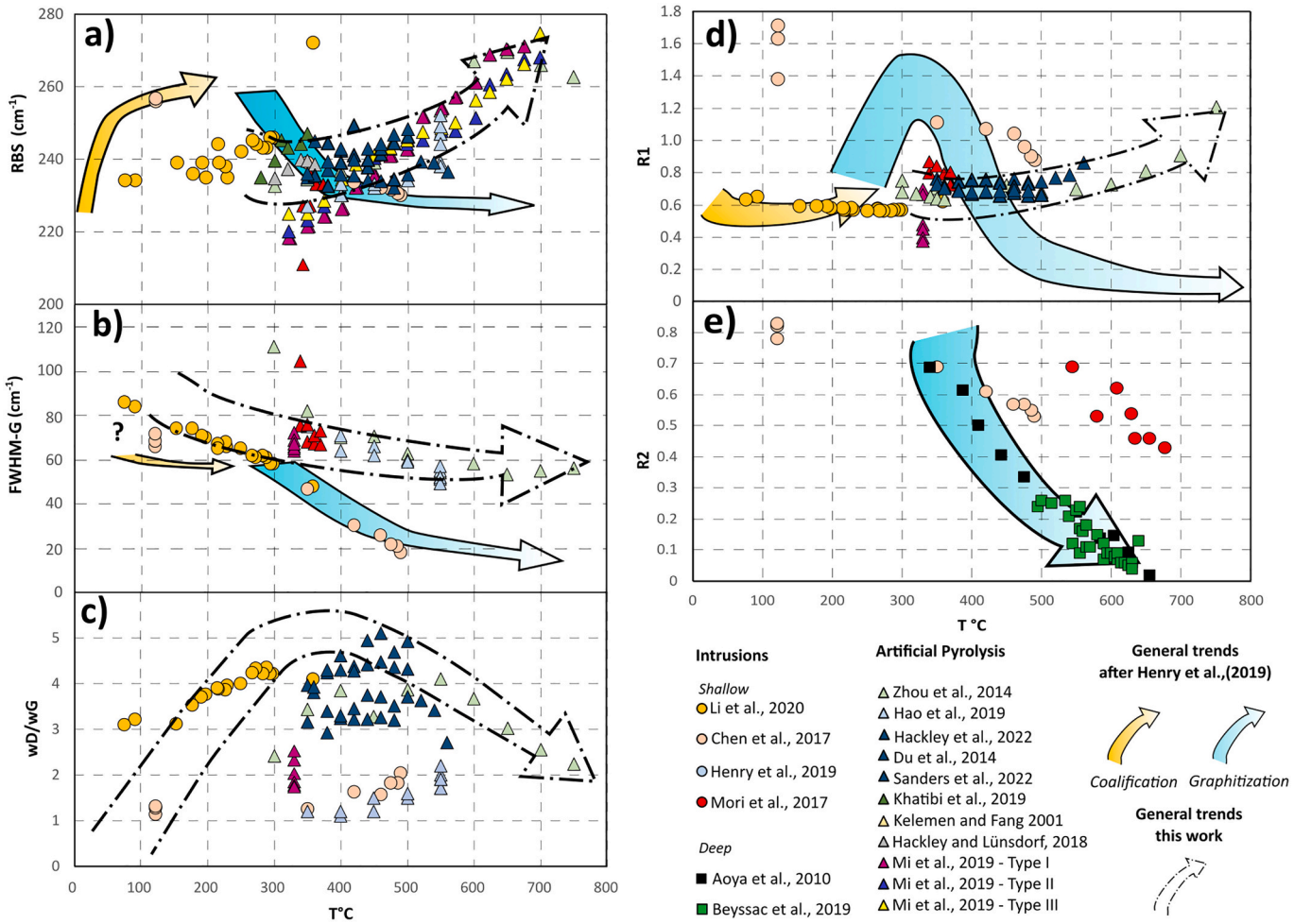

Fig. 4. Comparison of Raman parameters a) RBS, b) FWHM-G, c) wD/wG, d) R1 and e) R2, against temperatures around intrusions and artificial pyrolysis temperatures. Orange and blue arrows indicate general trends for coalification or graphitization found by Henry et al. (2019a); dotted arrows show the trends found in this work. Question mark in Fig. b indicates uncertainties in the FWHM-G values at low temperatures. The trend has been depicted by Henry et al. (2019a) against Ro % but correlation with temperatures is unclear. (For interpretation of the references to colour in this figure legend, the reader is referred to the web version of this article.)

et al., 2012; Wang, 2012; Iyer et al., 2013, 2017; Mori et al., 2017) since, as outlined by Wang et al. (2008), Ro% conversion using the Barker and Pawlewicz (1994) equation in contact metamorphism can lead to underestimation by >200 °C near the contact with the intrusion.

Pyrolysis temperatures can also be compared since the residence time of most of the experiments is similar (72 h; Fig. 4). Artificial maturation is generally performed between 300 and 600 °C while some work (Zhou et al., 2014) extends the range up to 750 °C.

Fig. 4a shows that the RBS parameter always shows a, more or less, linear increase with temperature (dotted arrow). Hydrous pyrolysis (Hackley and Lünsdorf, 2018; Khatibi et al., 2019; Hackley et al., 2022; Sanders et al., 2022) follows a similar trend for data of Li et al. (2020) (assuming their temperatures are underestimated). Even if based on fewer data, Figs. 4b,d shows that the "fast heating" trend (dotted arrows) roughly follow the same trend depicted by Henry et al. (2019a) but shifted toward higher temperatures. Moreover, Fig. 4e clearly shows the difference in R2 pattern for deep (Aoya et al., 2010; Beyssac et al., 2019) and shallow intrusions (Chen et al., 2017; Mori et al., 2017).

Comparing the new trends highlighted in Fig. 4 a-d with the general trend for coalification/graphitization (respectively orange and blue arrows), we suggest that pyrolyzed and shallow intrusion CM follow only the coalification trend and thus never achieve proper graphitization. Given this, the R2 parameter can be misleading if not used only to describe graphitization (Fig. 4 e).

Notably, especially in contact metamorphism, graphite precipitation from carbon-rich hydrothermal fluids (see Rumble, 2014 for a review) is common. This process, however, is not directly related to the metamorphic maximum temperatures rather to the redox redox state, pressure and temperature conditions of the fluids (Huizenga, 2011) and has thus not been considered in this review. Even if mainly observed at high metamorphic ranks (Luque and Rodas, 1999; Luque et al., 2009), fluid-precipitate-graphite at the contact with shallow intrusion has also been reported (Lindgren and Parnell, 2006).

4.2. *Raman shift in faulted rocks: Difference between seismic and aseismic slip*

Among all the uses of the Raman spectroscopy geothermometer, the application to faults and shear zones is the most controversial, and there is still an open debate on the impact on Raman spectral shift (Muirhead et al., 2021).

The researchers mentioned in Section 3.4 all work on low maturity kerogen or graphitic carbon, while Nakamura et al. (2015) and Kirilova et al. (2018) study the Raman ordering of graphite from cataclasite to slip plane, and in frictional experiments respectively.

These works evaluate different Raman parameters, but the most used are the R1 ratio and RBS for natural heating (Fig. 5 a,b) and experimental frictional heating (Fig. 5 c,d).

Hirono et al. (2015) and Mukoyoshi et al. (2018) work on low mature kerogen on both sides of main thrusts, the first in Chelungpu Fault (Taiwan) and the second in the Emi thrust and Kure out-of-sequence thrust (OST) in Japan. Hirono et al. (2015), find a slight increase in the R1 values and more marked increase in the RBS values (Fig. 5 a,b) toward the slip zone, and also after artificial shearing. An increase of the R1 ratio (Fig. 5 a) is also observed on graphitic carbon (i.e., carbon that suffered at least greenschist metamorphism) from Monti Romani (Italy) and Internal Rif (Morocco) by Muirhead et al. (2021) and by Ito et al. (2017). Working on zones of concentrated aseismic strain, other authors (Kuo et al., 2017 in low slip rate experiments; Kuo et al., 2018a, 2018b; Kedar et al., 2020, 2021; Muirhead et al., 2021) find a decrease of the R1 values (Fig. 5 a).

Apart from the uncertainties arising from the use of different Raman parameters, different fitting approaches (laser is mainly 514–532 cm^{-1}, see Table 3) or different preparation (thin section, CM concentration, clay-size deposited gouges on glass slides), most of the confusion is because authors deal with different carbonaceous material precursors (i.e., amorphous carbon, graphitic carbon or graphite) and usually do not discriminate between the effect of strain or frictional heating. Much work to date has focussed on understanding the increase of temperature on fault planes, with some experiments trying to reproduce the process (Hirono et al., 2015; Furuichi et al., 2015; Kuo et al., 2017; Ito et al., 2017, Mukoyoshi et al., 2018). Nevertheless, frictional and transient heating experiments should be compared only with samples collected on the slip plane (Ito et al., 2017) while enhanced maturation within the fault's damage zone (sensu *lato*) should be ascribed to the effect of strain, fluid circulation or the interplay of both (Muirhead et al., 2021). This is the case of the Raman shift of amorphous carbon (Fig. 5), ascribed to aseismic shear strain by Kedar et al. (2020, 2021) and Muirhead et al. (2021) and possibly in the damage, breccia and gouge zones of Hirono et al. (2015). From Fig. 5 the evolution of Raman parameters in these works is not straightforward, showing a simultaneous R1 low shift and RBS high shift (Fig. 5; Kedar et al., 2020; Muirhead et al., 2021). However, the R1 parameter in low diagenesis is known to have an uncertain trend (Schito et al., 2017; Schito and Corrado, 2020; Henry et al., 2019a), so it cannot definitively point to a thermal maturity increase or decrease. On the other hand, R1 and RBS increases observed in both natural and experimental samples strongly suggest enhanced maturation due to the effect of strain (Fig. 5).

On graphitic carbon in low-grade metamorphic conditions (Fig. 5), R1 increases in natural samples (Muirhead et al., 2021), suggesting a strain-related ordering, while in Kuo et al. (2017, 2018a, 2018b) simultaneous R1 decrease, and RBS increase reflect a similar behaviour of amorphous carbon described above. In graphite, on the other hand, R1 increases in both natural and experimental examples, suggesting an ordering decrease (Fig. 5; Nakamura et al., 2015; Kirilova et al., 2018) likely due to mechanical disruption of the graphite lattice (Kirilova

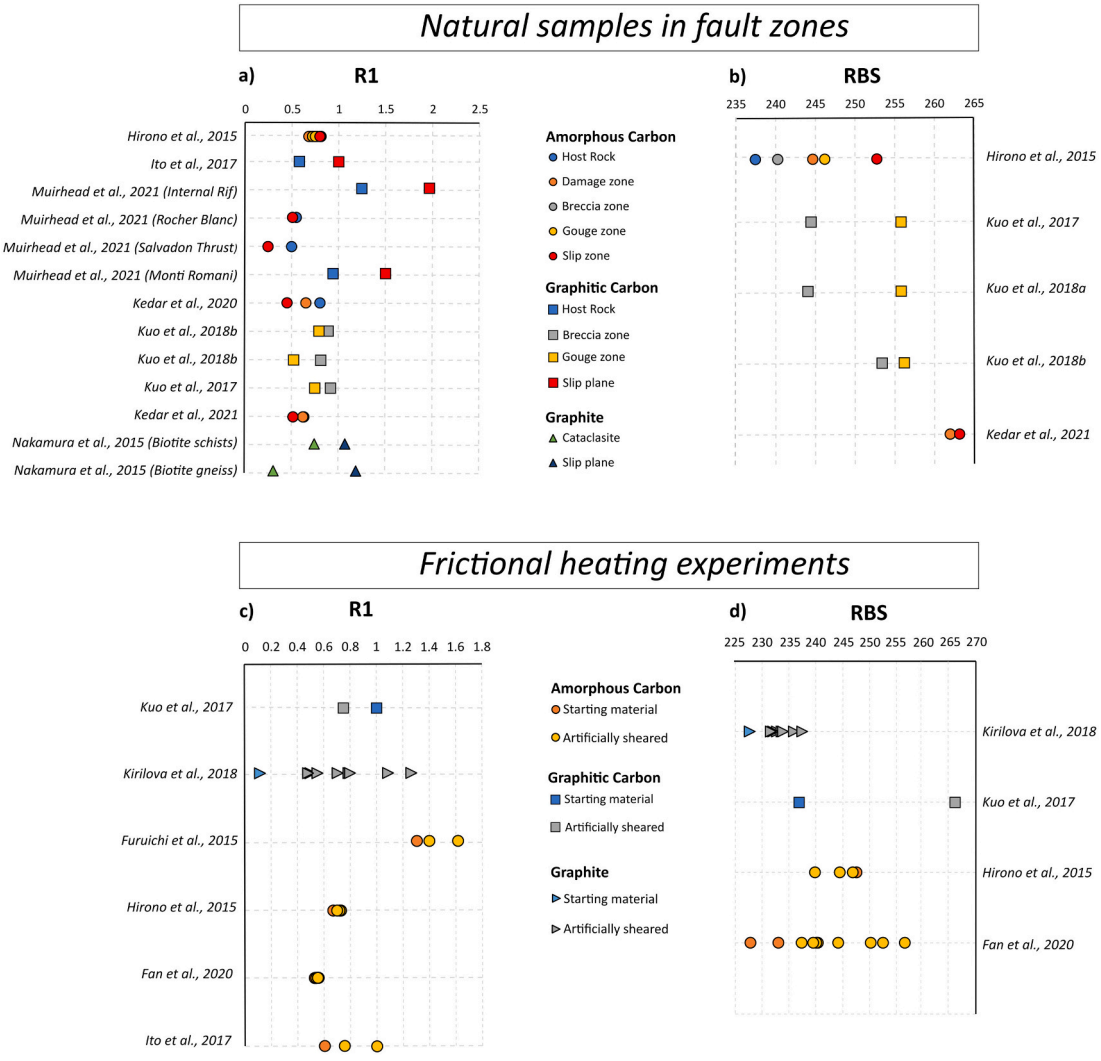

Fig. 5. Effect of strain and shear on ID/IG and RBS Raman parameters for natural samples collected at different distances from fault planes and artificially sheared samples.

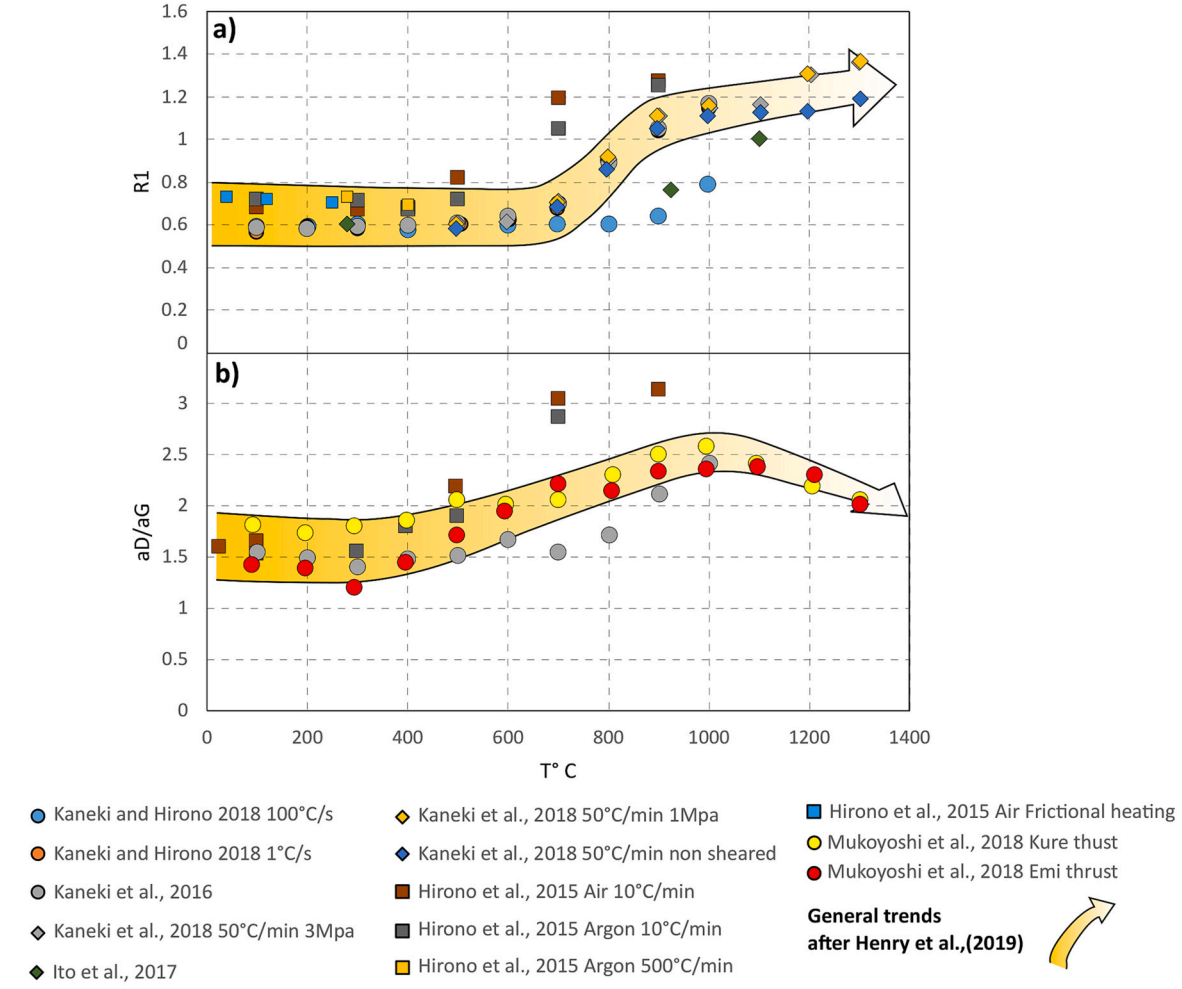

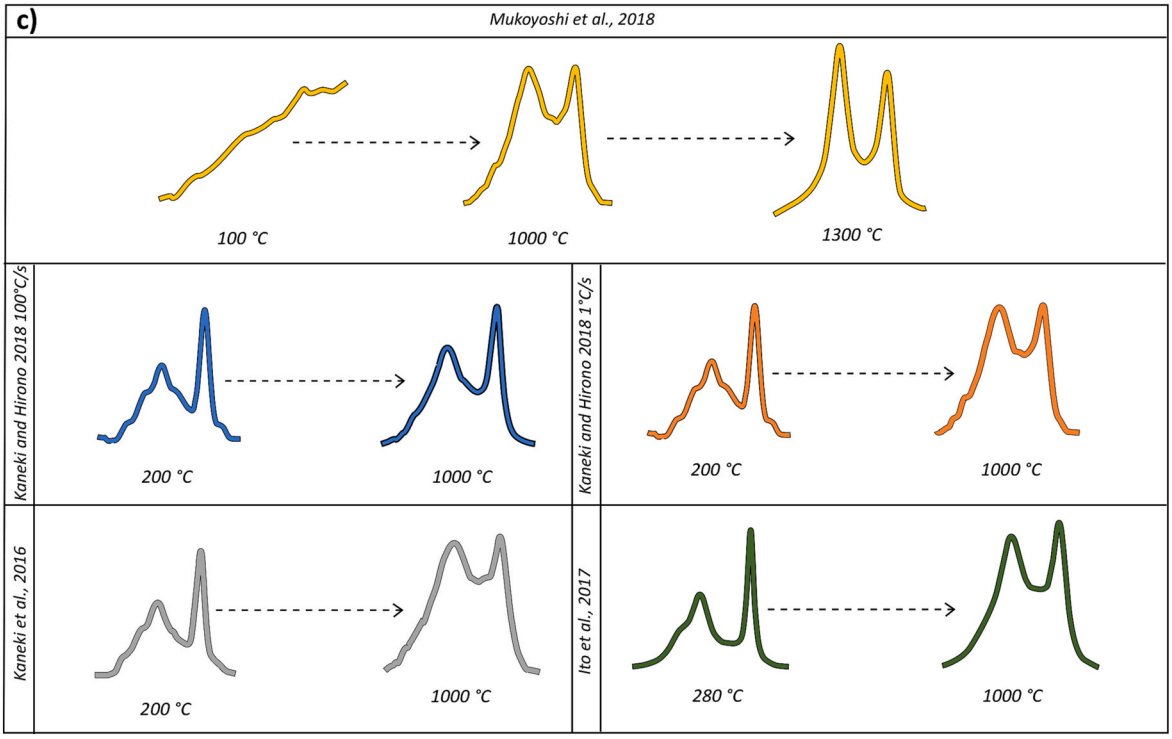

Fig. 6. a) R1 and b) aD/aG parameter for transient heating experiments and c) related spectra.

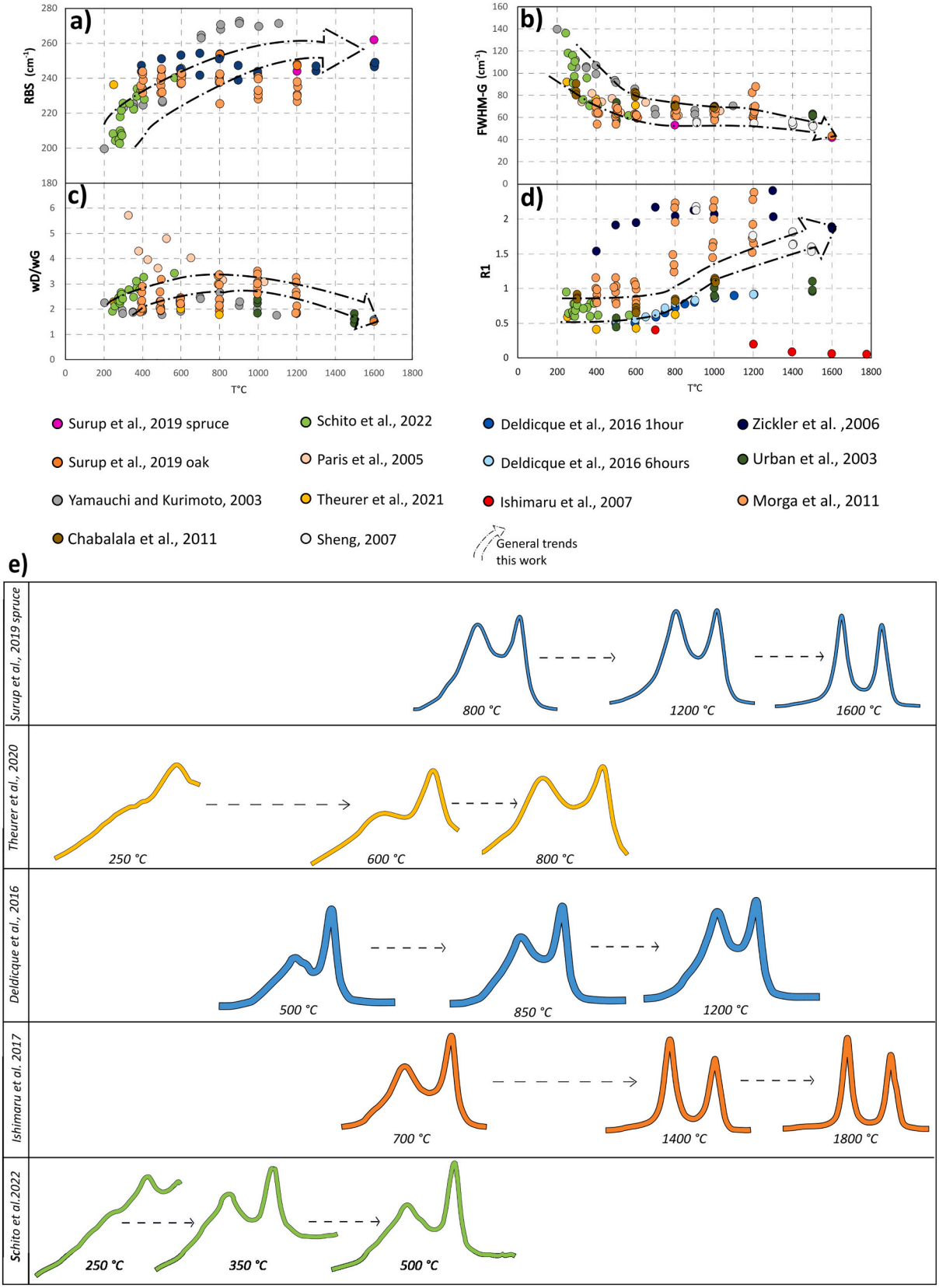

Fig. 7. Charcoal Raman parameters plotted against maximum temperatures. a) RBS; b) FWHM-G; c) wD/wG and d) R1 parameters. Fig. e) shows spectra evolution in experiments from Surup et al. (2019); Theurer et al. (2021); Deldicque et al. (2016) and Ishimaru et al. (2007); Schito et al. (2022). In Theurer et al. (2021) andSchito et al. (2022) spectra are shown without baseline subtraction.

et al., 2018). It is worth noting that in metamorphism, the R1 parameter first increases at greenschist facies and then decreases up to the graphite stage as shown by the blue arrow in Fig. 5. This behaviour is probably the cause of the apparent discrepancies in R1 in graphitic carbon (Fig. 5, Kuo et al., 2017, 2018a, 2018b; Muirhead et al., 2021).

Fig. 5, highlights that there are instances in the literature of strain-related induced maturation in both amorphous and graphitic carbon. Of particular interest is the work of Fan et al. (2020) that show the shift of the RBS parameter because of the increase of effective normal stress in friction isothermal experiments (Fig. 5 c,d) as already outlined by Maslova et al. (2012). This also seems to confirm the role of strain in the mismatch between spectra at the same maturity observed in Figs. 2 and 3.

Looking at the Raman shift in experiments, it can be observed that frictional heating by rotary shear, generally yield higher R1 values after shearing (Fig. 5 c; Furuichi et al., 2015; Hirono et al., 2015; Ito et a., 2017; Fan et al., 2020), except in the work of Kuo et al. (2017). Also, an increase in the RBS values (Fig. 5 a) is shown in shear experiments except from Hirono et al. (2015). On the other hand, the increase of the R1 and RBS values reported for graphite (Fig. 5 c,d) show how both brittle deformation in fault zones (Nakamura et al., 2015) or shearing at experimental sliding velocities reduce the ordering of graphite. The authors thus suggest caution when using the RSCM geothermometers in active tectonic settings.

Almost all the authors that performed frictional and/or transient heating experiment to calculate temperatures (Fig. 6), only the R1 and aG/aD parameters are used. As shown in Fig. 6a, R1 and aD/aG values remain mainly constant at low temperature, starting to increase at about 400 °C for low heating rates and after 800 °C heating rates higher than 1 °C/s. As well, the aD/aG parameter seems to only slightly increase up to 600 °C while between 600 and 1000 °C it shows a rapid increase and decrease for higher temperatures (Fig. 6 b). These trends have been already identified by Henry et al. (2019a) (coloured arrows in Fig. 6 a, b).

Looking at Fig. 6, some interesting issues raise. First of all, a flat initial R1 ratio is observed, similarly to what observed in diagenesis/metamorphism but at lower temperatures. In addition, the R1 parameter starts to raise at progressively higher temperatures depending on the heating rate conditions: samples from Hirono et al. (2015) burned at 10 °C/min (red and purple squares) start to increase at lower temperatures than samples burned at 50 °C/min (about 1 °C/s) from Kaneki et al. (2018; diamonds) and Kaneki and Hirono (2018; orange circles) and samples heated at 100 °C/s (Kaneki and Hirono, 2018; blue circles) only slightly increase after 900 °*C*. Ito et al. (2017) do not specify their heating rate but state they achieve maximum temperatures of >1000 °C in a few seconds to properly simulate frictional heating during earthquakes (Kaneki et al., 2016).

Accordingly, the enhanced maturation due to seismic frictional heating implies very high temperatures reached in a very short amount of time and is thus comparable to a flash pyrolysis (Muirhead et al., 2012; Ito et al., 2017; Aubry et al., 2018) leading to the trends and spectra shape of Fig. 6. Spectra drawn in Fig. 6 c, in particular, show high intensities in the valley between the D and G bands that start to drop after 1000 °C (Fig. 6 c). These spectra are different from those show in Figs. 2 and 3 suggesting a very different evolution path. The most outstanding evidence from these experiments is the apparent "disordering" shift in spectra in Fig. 6e. Here, spectra that already achieved a low-metamorphic ordering seem to transform into very disordered ones at high temperatures. The use of the term ordering is thus here misleading since the Raman shift is showing a "jump" from a diagenetic/metamorphic path up to another at higher heating rates.

4.3. Charcoal Raman spectra

The application to charcoal geothermometry is probably the most recent advance, and has shown attractive potential application in archaeological, paleo-environmental and geological studies (Deldicque and Rouzaud, 2020; Mauquoy et al., 2020; Theurer et al., 2021, 2022; Schito et al., 2022) as well as for industrial application (Surup et al., 2019). Such large spectrum of applications results in a wide range of temperatures used in calibration experiments, up to almost 2000 °C. Most of the results shown in Fig. 7 derive from artificial heating (except Schito et al., 2022).

As shown by the dotted arrow in Fig. 7a, the RBS parameter shows an increase from about 200 to 1100 °C and a further increase is also observed at higher temperatures by Surup et al. (2019), Zickler et al. (2006) and Urban et al. (2003). It is worth noting that Yamauchi and Kurimoto (2003) performed their Raman experiments using a red (632 cm^{-1}) laser and a power output of 220 mW. As discusses above, this imply an overestimation of D band related parameter (Kouketsu et al., 2014; Lünsdorf, 2016) and thus imply RBS shift toward higher values with respect to data from all the other authors that use a green (514 or 532 cm^{-1}) laser. Moreover, thermal degradation due to the high laser intensity for low temperature samples cannot be excluded, as evidenced by the work of Henry et al. (2018).

The FWHM-G parameter also shows a continue decrease over the whole temperatures range (Fig. 7b), while an increase of the wD/wG values up to 800 °C was observed by Yamauchi and Kurimoto (2003) and Schito et al. (2022) that is the opposite of what Paris et al. (2005) and Theurer et al. (2021) observed (Fig. 7c). Finally, the R1 values show an increase only from 500 to 1200 °C, followed by a decrease up to 1800 °C.

The "transient heating" Raman parameters trends (dotted arrows) in Figs. 6 and 7 can sometimes resemble those from Figs. 2 a-d and 3 a-b but this can be highly misleading since spectra evolution is entirely different as shown in Figs. 2 e, 3 c, 6c and 7e.

Spectra shown in Fig. 7e point out that only low-temperature (perhaps below 600 °C) spectra are similar to those observed in diagenetic samples (Fig. 2) or in pyrolysis experiments (see Fig. 3). Conversely, high temperatures spectra are all characterized by high intensities in the valley between the D and G bands and mostly resemble those ones from Fig. 6. This is because of similar experimental conditions. Accordingly, in these transient heating trend (charcoalification) an increase of the D band intensity with respect to the G band is observed, up the R1 ratio reaches a value of about 1 at 1200 °C (Fig. 7 d, e). After that, a decrease of the valley intensities, after perhaps 1600 °C, led to spectra's shape similar to those of greenschist facies. Thermal graphitization is never achieved in these experiments but it is known from literature to be generally achieved at temperatures higher than 2200 °C (Bonijoly et al., 1982).

5. Kinetic effects and future perspectives

The mismatches of Raman parameters against Ro% discussed in Section 4.1 indicate that these analytical approaches measure different processes. Both measures correlate to the increase of aromatic organic matter at increasing temperature, but at non-linear rates as already outlined by Carr and Williamson (1990). This review outlines that differences in maturation rates are enhanced when compared different heating regimes and that at increasing heating rates aromaticity increase proceed at a slower rate than vitrinite reflectance increase (Figs. 2 and 3). It is also possible that the spatial higher resolution of the laser spot in Raman spectroscopy is able to detect more precise characteristics of the molecular arrangement then those that lead to the reflectance increase on the surface of the organic material. This implies that, if Raman measurements are to be used in thermal modelling, the use of Ro% kinetics is not appropriate,and a new model based on Raman parameters needs to be developed. It has been argued that heating rate and strain can influence spectral evolution and thus their effects should be included in the kinetic model.

Additionally, in studies to date, the most used kinetic model for organic matter maturation has been the Sweeney and Burnham (1990)

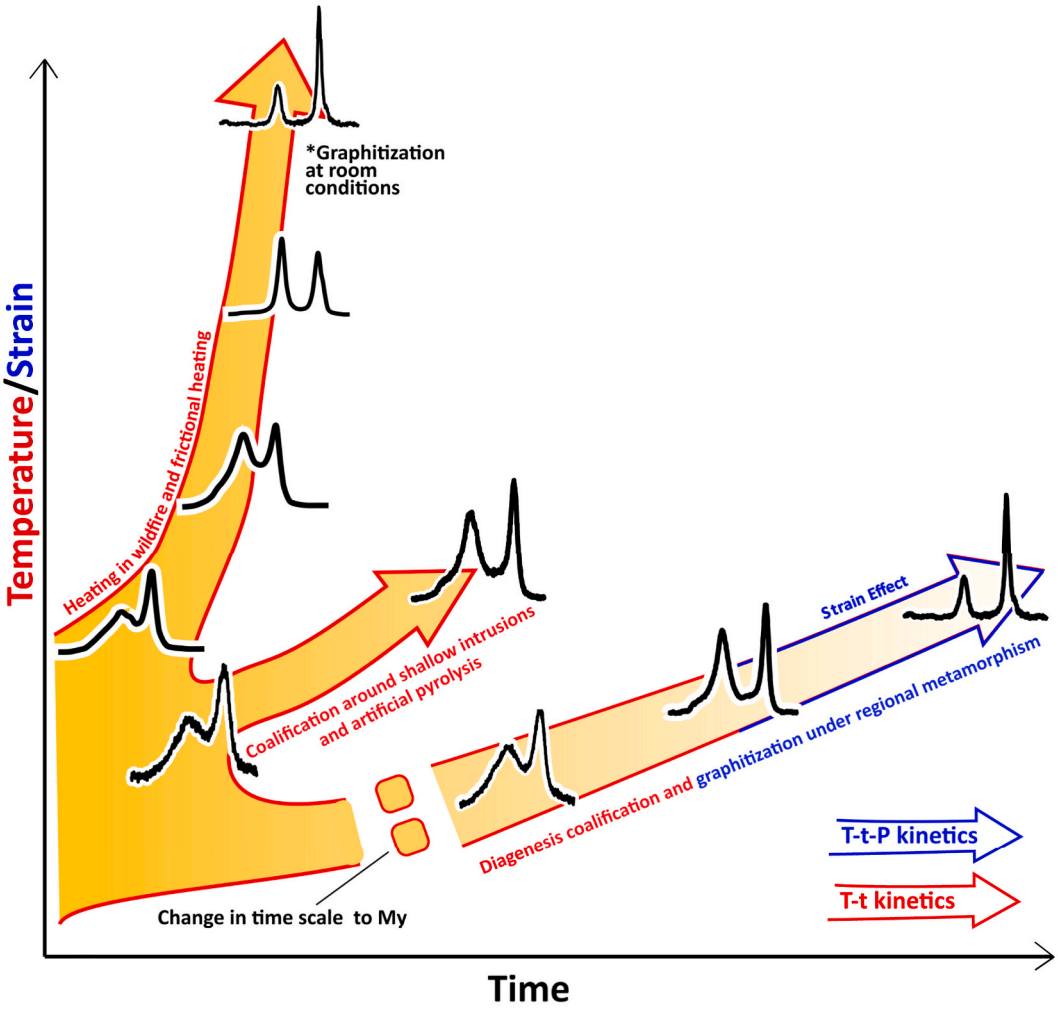

Fig. 8. Schematic Raman spectra evolution as a function of temperature, time and strain. Not in scale. The interrupted arrow in the diagenesis /regional metamorphism path highlight the switch of the time scale from hours-days-years up to million years. The red colour indicate the path that can be modelled with a T-t kinetics, the blue those can be modelled by using a T-t-P kinetics. *Graphitization at room conditions cannot be achieved under natural conditions. (For interpretation of the references to colour in this figure legend, the reader is referred to the web version of this article.)

model ($EASYR_O$%) that has been recently revised by Burnham (2019) to include models for different kerogen types. Recent alternatives have been also proposed by Nielsen et al. (2017) and Wood (2018). These models allow the user to reproduce an increase of vitrinite reflectance as a function of temperature and time by using an Arrhenius equation and assuming that organic matter maturation can be simply treated by considering four independent parallel reactions that in turn eliminate water and carbon dioxide during early maturation and heavy to light hydrocarbons in the later stages. In the $EASYR_O$% model of Sweeney and Burnham (1990) and Burnham (2019), the Arrhenius equation is based on a single frequency factor and a distribution of activation energies for each one of the parallel reactions. Activation energies rise, up to known values at the metagenetic stage. After that, the turbostratic structure of anthracite starts to form, and in the graphitization process of natural anthracite the same kinetic parameters cannot be used, since lithostatic pressure starts to play a fundamental role in promoting the accumulation of strain energy needed to mechanically reorientate and align the aromatic units until defect-free aromatic sheets of triperiodic graphite form (Bonijoly et al., 1982; Bustin et al., 1995; Lünsdorf, 2016). It has been demonstrated that the role of pressure is to lower the activation energies required for the graphitization process and a kinetic control for graphitization, in which the role of pressure is considered, has been provided by Nakamura et al. (2017, 2020), but can be applied only in high metamorphism. The next step in this area of research will be to understand when the role of pressure must be included at the boundary between high diagenesis and low metamorphism. Other outcomes on this topic, derive from the experiments made by Huang et al. (2010) using a sapphire anvil cell connected to the Raman apparatus. Their data show a transient effect of differential pressure of Raman spectra that disappear after the stress is released. This is interesting evidence, that, together with the work of Khatibi et al. (2018) on the relation between CM Raman spectrum and the Young's modulus can pave the ground for future studies.

This review has also demonstrated that there are natural conditions of heating, such as charring on fault planes or in wildfires, where the evolution of Raman spectra follow different paths. Such an effect can also be described by means of a kinetic approach. Based on experiments performed mainly in the 1990s, it was observed that artificial graphitization at room temperature requires temperatures higher than 1700 °C (depending on the precursor material) and activation energies too high to be achieved in natural conditions (Ross and Bustin, 1990; Ross et al., 1991). Given this, we can assume that the activation energies necessary to generate the charcoals (spectra shown in Figs. 5e-i and 7 c-g) are higher than those needed to generate graphitic carbon under metamorphic conditions. In this way the temperature-driven "apparent" disordering trend observed in Fig. 6e can be explained and the co-existence of graphitic carbon and charcoal-like carbon could be predicted in a faulted rock.

The evolution of carbonaceous material in natural conditions can be summarized as a function of their temperatures, the effects of time (consequently the heating rate) and those of strain (i.e. pressure). All these factors act on the activation energy and three main paths of Raman evolution can be recognized accordingly (Fig. 8): 1) a low temperature path where coalification and then graphitization are mainly driven by the temperature and the strain during metamorphism that keep low activation energies as demonstrated by Nakamura et al. (2017, 2020). Note that the boundary at which strain starts to have an effect is still not known but will probably lie at the low metamorphism onset; 2) a similar path but at higher temperatures and on different time scale, that represents coalification around (shallow) intrusions and in artificial pyrolysis 3) a high temperature/high heating rate (also implying high activation energy) path where high temperature charcoals can be formed as a consequence of transient heating as in wildfires or friction along fault slip planes.

The red or blue colours in Fig. 8 indicate the kinetics that would be able to describe the all these paths showing schematically where it could a T-t or a T-t-P based kinetics.

Based on these assumptions, calibrating a kinetic model with Raman parameters would be able to describe almost every condition of carbonaceous material maturation that can be found in natural systems.

6. Conclusions

A new updated review on the behaviour of Raman spectrum of CM under different maturation conditions highlights the need for a kinetic model for different heating rates that can be found in natural systems. The main conclusions are that:

1) There is a mismatch between Raman spectra at the same maturities between fast and slow heating rates;
2) Such differences are probably due to the interplay of different (other than Ro%) kinetics and pressure;
3) Both strain and frictional heating can affect CM spectra in highly deformed rocks, nevertheless, they need to be distinguished since they follow a different path;
4) Charcoals and artificial frictional heating experiments generate similar spectra. However, the kinetics of the process need to be understood;
5) Building a kinetic model based on Raman spectra would provide a universal geothermometer for CM in geological studies.

Declaration of Competing Interest

The authors declare that they have no known competing financial interests or personal relationships that could have appeared to influence the work reported in this paper.

Data availability

Data will be made available on request.

7Acknowledgements

This work was funded by the School of Geosciences, University of Aberdeen. Stimulating discussion with Sveva Corrado and Thomas Theurer greatly enriched this work. The Editor Shuhab Khan, the reviewer Aaron Jubb and two anonymous reviewers are kindly acknowledged for their comments that significantly improve the original version of the manuscript.

References

Aarnes, I., Svensen, H., Polteau, S., Planke, S., 2011. Contact metamorphic devolatilization of shales in the Karoo Basin, South Africa, and the effects of multiple sill intrusions. Chem. Geol. 281 (3-4), 181–194. https://doi.org/10.1016/j.chemgeo.2010.12.007.

Allen, P., Allen, J., 2013. Basin Analysis: Principles and Application to Petroleum Play Assessment, third ed. Wiley Blackwell, New York.

Amari, S., Anders, E., Virag, A., Zinner, E., 1990. Interstellar graphite in meteorites. Nature 345 (6272), 238–240.

Aoya, M., Kouketsu, Y., Endo, S., Shimizu, H., Mizukami, T., Nakamura, D., Wallis, S., 2010. Extending the applicability of the Raman carbonaceous-material geothermometer using data from contact metamorphic rocks. J. Metamorph. Geol. 28 (9), 859–914. https://doi.org/10.1111/j.1525-1314.2010.00896.x.

Aretusini, S., Núñez-Cascajero, A., Spagnuolo, E., Tapetado, A., Vázquez, C., Di Toro, G., 2021. Fast and localized temperature measurements during simulated earthquakes in carbonate rocks. Geophys. Res. Lett. 48 (9) https://doi.org/10.1029/2020GL091856 e2020GL091856.

Ascough, P.L., Bird, M.I., Scott, A.C., Collinson, M.E., Cohen-Ofri, I., Snape, C.E., Le Manquais, K., 2010. Charcoal reflectance measurements: implications for structural characterization and assessment of diagenetic alteration. J. Archaeol. Sci. 37 (7), 1590–1599. https://doi.org/10.1016/j.jas.2010.01.020.

Aubry, J., Passelègue, F.X., Deldicque, D., Girault, F., Marty, S., Lahfid, A., Bhat, H., Escartin, J., Schubnel, A., 2018. Frictional heating processes and energy budget during laboratory earthquakes. Geophys. Res. Lett. 45 (22), 12–274. https://doi.org/10.1029/2018GL079263.

Barker, C.E., Pawlewicz, M.J., 1994. Calculation of vitrinite reflectance from thermal histories and peak temperatures. In: Mukhopadhyay, P.K., Dow, W.G. (Eds.), Vitrinite Reflectance as a Maturity Parameter, Applications and Limitations, Washington DC, pp. 216–229. https://doi.org/10.1021/bk-1994-0570.ch014.

Barzoi, S.C., 2015. Shear stress in the graphitization of carbonaceous matter during the low-grade metamorphism from the northern Parang Mountains (South Carpathians)—Implications to graphite geothermometry. Int. J. Coal Geol. 146, 179–187. https://doi.org/10.1016/j.coal.2015.05.008.

Beny-Bassez, C., Rouzaud, J.N., 1984. Characterization of carbonaceous materials by correlated electron and optical microscopy and Raman microspectroscopy. Scan. Electron Microsc. 1985 (1), 11, 119-132.

Beyssac, O., Goffé, B., Petitet, J.P., Froigneux, E., Moreau, M., Rouzaud, J.N., 2003. On the characterization of disordered and heterogeneous carbonaceous materials by Raman spectroscopy. Spectrochimica Acta Part A: Molecular and Biomolecular Spectroscopy 59 (10), 2267–2276. https://doi.org/10.1016/S1386-1425(03)00070-2.

Beyssac, O., Rumble, D., 2014. Graphitic carbon: a ubiquitous, diverse, and useful geomaterial. Elements 10 (6), 415–420. https://doi.org/10.2113/gselements.10.6.415.

Beyssac, O., Goffé, B., Chopin, C., Rouzaud, J.N., 2002. Raman spectra of carbonaceous material in metasediments: a new geothermometer. J. Metamorph. Geol. 20 (9), 859–871. https://doi.org/10.1046/j.1525-1314.2002.00408.x.

Beyssac, O., Pattison, D.R.M., Bourdelle, F., 2019. Contrasting degrees of recrystallization of carbonaceous material in the Nelson aureole, British Columbia and Ballachulish aureole, Scotland, with implications for thermometry based on Raman spectroscopy of carbonaceous material. J. Metamorph. Geol. 37 (1), 71–95. https://doi.org/10.1111/jmg.12449.

Birdwell, J.E., Jubb, A.M., Hackley, P.C., Hatcherian, J.J., 2021. Compositional evolution of organic matter in Boquillas Shale across a thermal gradient at the single particle level. Int. J. Coal Geol. 248, 103859 https://doi.org/10.1016/j.fuel.2018.01.107.

Bonijoly, M., Oberlin, M., Oberlin, A., 1982. A possible mechanism for natural graphite formation. Int. J. Coal Geol. 1 (4), 283–312. https://doi.org/10.1016/0166-5162(82)90018-0.

Bonoldi, L., di Paolo, L., Flego, C., 2016. Vibrational spectroscopy assessment of kerogen maturity in organic-rich source rocks. Vib. Spectrosc. 87, 14–19. https://doi.org/10.1016/j.vibspec.2016.08.014.

Bostick, N.H., Pawlewicz, M.J., 1984. Paleotemperatures based on vitrinite reflectance of shales and limestones in igneous dike aureoles in the upper cretaceous Pierre shale, Walsenburg, Colorado. In: Woodward, J., Meissner, F.F., Clayton, J.L. (Eds.), Hydrocarbon Source Rocks of the Greater Rocky Mountain Region, Denver, pp. 387–392.

Brolly, C., Parnell, J., Bowden, S., 2017. Raman spectroscopy of shocked gypsum from a meteorite impact crater. Int. J. Astrobiol. 16 (3), 286–292. https://doi.org/10.1017/S1473550416000367.

Burnham, A.K., 2019. Kinetic models of vitrinite, kerogen, and bitumen reflectance. Org. Geochem. 131, 50–59. https://doi.org/10.1016/j.orggeochem.2019.03.007.

Bustin, R.M., Ross, J.V., Rouzaud, J.N., 1995. Mechanisms of graphite formation from kerogen: experimental evidence. Int. J. Coal Geol. 28 (1), 1–36. https://doi.org/10.1016/0166-5162(95)00002-U.

Carr, A.D., Williamson, J.E., 1990. The relationship between aromaticity, vitrinite reflectance and maceral composition of coals: implications for the use of vitrinite reflectance as a maturation parameter. Org. Geochem. 16 (1–3), 313–323. https://doi.org/10.1016/0146-6380(90)90051-Z.

Castiglioni, C., Tommasini, M., Zerbi, G., 2004. Raman spectroscopy of polyconjugated molecules and materials: confinement effect in one and two dimensions. Philos. Trans. R. Soc. A Math. Phys. Eng. Sci. 362 (1824), 2425–2459. https://doi.org/10.1098/rsta.2004.1448.

Chabalala, V.P., Wagner, N., Potgieter-Vermaak, S., 2011. Investigation into the evolution of char structure using Raman spectroscopy in conjunction with coal petrography; Part 1. Fuel Process. Technol. 92 (4), 750–756. https://doi.org/10.1016/j.fuproc.2010.09.006.

Chen, S., Wu, D., Liu, G., Sun, R., 2017. Raman spectral characteristics of magmatic-contact metamorphic coals from Huainan Coalfield, China. Spectrochim. Acta Part A: Mol. Biomol. Spectrosc. 171, 31–39. https://doi.org/10.1016/j.saa.2016.07.032.

Corrado, S., Schito, A., Romano, C., Grigo, D., Poe, B.T., Aldega, L., Caricchi, C., Di Paolo, L., Zattin, M., 2020. An integrated platform for thermal maturity assessment of polyphase, long-lasting sedimentary basins, from classical to brand-new thermal parameters and models: an example from the on-shore Baltic Basin (Poland). Mar. Pet. Geol. 122, 104547 https://doi.org/10.1016/j.marpetgeo.2020.104547.

Deldicque, D., Rouzaud, J.N., 2020. Temperatures reached by the roof structure of Notre-Dame de Paris in the fire of April 15th 2019 determined by Raman paleothermometry. Comptes Rendus. Géoscience 352 (1), 7–18. https://doi.org/10.5802/crgeos.9.

Deldicque, D., Rouzaud, J.N., Velde, B., 2016. A Raman - HRTEM study of the carbonization of wood: A new Raman-based paleothermometer dedicated to archaeometry. Carbon 102, 319–329. https://doi.org/10.1016/j.carbon.2016.02.042.

Du, J., Geng, A., Liao, Z., Cheng, B., 2014. Potential Raman parameters to assess the thermal evolution of kerogens from different pyrolysis experiments. J. Anal. Appl. Pyrolysis 107, 242–249. https://doi.org/10.1016/j.jaap.2014.03.007.

Fan, C., Liu, J., Hunfeld, L.B., Spiers, C.J., 2020. Frictional slip weakening and shear-enhanced crystallinity in simulated coal fault gouges at slow slip rates. Solid Earth 11 (4), 1399–1422. https://doi.org/10.5194/se-11-1399-2020.

Ferralis, N., Matys, E.D., Knoll, A.H., Hallmann, C., Summons, R.E., 2016. Rapid, direct and non-destructive assessment of fossil organic matter via microRaman spectroscopy. Carbon 108, 440–449. https://doi.org/10.1016/j.carbon.2016.07.039.

Ferrari, A.C., Robertson, J., 2000. Interpretation of Raman spectra of disordered and amorphous carbon. Phys. Rev. B 61 (20), 14095. https://doi.org/10.1103/PhysRevB.61.14095.

Furuichi, H., Ujiie, K., Kouketsu, Y., Saito, T., Tsutsumi, A., Wallis, S., 2015. Vitrinite reflectance and Raman spectra of carbonaceous material as indicators of frictional heating on faults: constraints from friction experiments. Earth Planet. Sci. Lett. 424, 191–200. https://doi.org/10.1016/j.epsl.2015.05.037.

Galushkin, Y.I., 1997. Thermal effects of igneous intrusions on maturity of organic matter: a possible mechanism of intrusion. Org. Geochem. 26 (11-12), 645–658. https://doi.org/10.1016/S0146-6380(97)00030-2.

Galvez, M.E., Beyssac, O., Martinez, I., Benzerara, K., Chaduteau, C., Malvoisin, B., Malavieille, J., 2013. Graphite formation by carbonate reduction during subduction. Nat. Geosci. 6 (6), 473–477. https://doi.org/10.1038/NGEO1827.

Guedes, A., Valentim, B., Prieto, A.C., Rodrigues, S., Noronha, F., 2010. Micro-Raman spectroscopy of collotelinite, fusinite and macrinite. Int. J. Coal Geol. 83, 415–422. https://doi.org/10.1016/j.coal.2010.06.002.

Hackley, P.C., Lünsdorf, N.K., 2018. Application of Raman spectroscopy as thermal maturity probe in shale petroleum systems: insights from natural and artificial maturation series. Energy Fuel 32 (11), 11190–11202. https://doi.org/10.1021/acs.energyfuels.8b02171.

Hackley, P.C., Jubb, A.M., Smith, P.L., McAleer, R.J., Valentine, B.J., Hatcherian, J.J., Botterell, P.J., Birdwell, J.E., 2022. Evaluating aromatization of solid bitumen generated in the presence and absence of water: Implications for solid bitumen reflectance as a thermal proxy. Int. J. Coal Geol. 258, 104016 https://doi.org/10.1016/j.coal.2022.104016.

Hao, J., Zhong, N., Luo, Q., Liu, D., Wu, J., Liu, A., 2019. Raman spectroscopy of graptolite periderm and its potential as an organic maturity indicator for the Lower Paleozoic in southwestern China. Int. J. Coal Geol. 213, 103278 https://doi.org/10.1016/j.coal.2019.103278.

Henry, D.G., Jarvis, I., Gillmore, G., Stephenson, M., Emmings, J.F., 2018. Assessing low-maturity organic matter in shales using Raman spectroscopy: effects of sample preparation and operating procedure. Int. J. Coal Geol. 191, 135–151. https://doi.org/10.1016/j.coal.2018.03.005.

Henry, D.G., Jarvis, I., Gillmore, G., Stephenson, M., 2019a. Raman spectroscopy as a tool to determine the thermal maturity of organic matter: application to sedimentary, metamorphic and structural geology. Earth Sci. Rev. 198, 102936 https://doi.org/10.1016/j.earscirev.2019.102936.

Henry, D.G., Jarvis, I., Gillmore, G., Stephenson, M., 2019b. A rapid method for determining organic matter maturity using Raman spectroscopy: application to Carboniferous organic-rich mudstones and coals. Int. J. Coal Geol. 203, 87–98. https://doi.org/10.1016/j.coal.2019.01.003.

Hilchie, L.J., Jamieson, R.A., 2014. Graphite thermometry in a low-pressure contact aureole, Halifax, Nova Scotia. Lithos 208, 21–33. https://doi.org/10.1016/j.lithos.2014.08.015.

Hirono, T., Maekawa, Y., Yabuta, H., 2015. Investigation of the records of earthquake slip in carbonaceous materials from the Taiwan Chelungpu fault by means of infrared and Raman spectroscopies. Geochem. Geophys. Geosyst. 16 (5), 1233–1253. https://doi.org/10.1002/2014GC005622.

Huang, E.P., Huang, E., Yu, S.C., Chen, Y.H., Lee, J.S., Fang, J.N., 2010. In situ Raman spectroscopy on kerogen at high temperatures and high pressures. Phys. Chem. Miner. 37 (9), 593–600. https://doi.org/10.1007/s00269-010-0360-9.

Huizenga, J.M., 2011. Thermodynamic modelling of a cooling C–O–H fluid–graphite system: implications for hydrothermal graphite precipitation. Mineral. Deposita 46 (1), 23–33. https://doi.org/10.1007/s00126-010-0310-y.

Hunt, J.M., 1995. Petroleum Geochemistry and Geology (Textbook). *Petroleum Geochemistry and Geology*, 2nd Ed. WH Freeman Company, New York, p. 332.

Ishimaru, K., Hata, T., Bronsveld, P., Nishizawa, T., Imamura, Y., 2007. Characterization of sp2-and sp3-bonded carbon in wood charcoal. J. Wood Sci. 53 (5), 442–448. https://doi.org/10.1007/s10086-007-0879-7.

Ito, K., Ujiie, K., Kagi, H., 2017. Detection of increased heating and estimation of coseismic shear stress from Raman spectra of carbonaceous material in pseudotachylytes. Geophys. Res. Lett. 44 (4), 1749–1757. https://doi.org/10.1002/2016GL072457.

Iyer, K., Rüpke, L., Galerne, C.Y., 2013. Modeling fluid flow in sedimentary basins with sill intrusions: implications for hydrothermal venting and climate change. Geochem. Geophys. Geosyst. 14 (1), 5244–5262. https://doi.org/10.1002/2013GC005012.

Iyer, K., Schmid, D.W., Planke, S., Millett, J., 2017. Modelling hydrothermal venting in volcanic sedimentary basins: Impact on hydrocarbon maturation and paleoclimate. Earth Planet. Sci. Lett. 467, 30–42. https://doi.org/10.1016/j.epsl.2017.03.023.

Iyer, K., Svensen, H., Schmid, D.W., 2018. SILLi 1.0: A 1-D numerical tool quantifying the thermal effects of sill intrusions. Geosci. Model Dev. 11 (1), 43–60. https://doi.org/10.5194/gmd-11-43-2018.

Kaneki, S., Hirono, T., 2018. Kinetic effect of heating rate on the thermal maturity of carbonaceous material as an indicator of frictional heat during earthquakes. Earth Planets Space 70 (1), 1–10. https://doi.org/10.1186/s40623-018-0868-7.

Kaneki, S., Hirono, T., Mukoyoshi, H., Sampei, Y., Ikehara, M., 2016. Organochemical characteristics of carbonaceous materials as indicators of heat recorded on an ancient plate-subduction fault. Geochem. Geophys. Geosyst. 17 (7), 2855–2868. https://doi.org/10.1002/2016GC006368.

Kaneki, S., Ichiba, T., Hirono, T., 2018. Mechanochemical effect on maturation of carbonaceous material: implications for thermal maturity as a proxy for temperature in estimation of coseismic slip parameters. Geophys. Res. Lett. 45 (5), 2248–2256. https://doi.org/10.1002/2017GL076791.

Kedar, L., Bond, C.E., Muirhead, D., 2020. Carbon ordering in an aseismic shear zone: implications for Raman geothermometry and strain tracking. Earth Planet. Sci. Lett. 549, 116536 https://doi.org/10.1016/j.epsl.2020.116536.

Kedar, L., Bond, C.E., Muirhead, D., 2021. Raman spectroscopy in thrust-stacked carbonates: an investigation of spectral parameters with implications for temperature calculations in strained samples. Solid Earth 13 (9), 1495–1511. https://doi.org/10.5194/se-2021-70.

Kelemen, S.R., Fang, H.L., 2001. Maturity trends in Raman spectra from kerogen and coal. Energy Fuel 15 (3), 653–658. https://doi.org/10.1021/ef0002039.

Khatibi, S., Ostadhassan, M., Tuschel, D., Gentzis, T., Bubach, B., Carvajal-Ortiz, H., 2018. Raman spectroscopy to study thermal maturity and elastic modulus of kerogen. Int. J. Coal Geol. 185, 103–118. https://doi.org/10.1016/j.coal.2017.11.008.

Khatibi, S., Ostadhassan, M., Hackley, P., Tuschel, D., Abarghani, A., Bubach, B., 2019. Understanding organic matter heterogeneity and maturation rate by Raman spectroscopy. Int. J. Coal Geol. 206, 46–64. https://doi.org/10.1016/j.coal.2019.03.009.

Kirilova, M., Toy, V., Rooney, J.S., Giorgetti, C., Gordon, K.C., Collettini, C., Takeshita, T., 2018. Structural disorder of graphite and implications for graphite thermometry. Solid Earth 9 (1), 223–231. https://doi.org/10.5194/se-9-223-2018.

Kitamura, M., Mukoyoshi, H., Fulton, P.M., Hirose, T., 2012. Coal maturation by frictional heat during rapid fault slip. Geophys. Res. Lett. 39 (16), L16302. https://doi.org/10.1029/2012GL052316.

Kouketsu, Y., Mizukami, T., Mori, H., Endo, S., Aoya, M., Hara, H., Nakamura, D., Wallis, S., 2014. A new approach to develop the Raman carbonaceous material geothermometer for low-grade metamorphism using peak width. Island Arc 23 (1), 33–50. https://doi.org/10.1111/iar.12057.

Kouketsu, Y., Shimizu, I., Wang, Y., Yao, L., Ma, S., Shimamoto, T., 2017. Raman spectra of carbonaceous materials in a fault zone in the Longmenshan thrust belt, China; comparisons with those of sedimentary and metamorphic rocks. Tectonophysics 699, 129–145. https://doi.org/10.1016/j.tecto.2017.01.015.

Kuo, L.W., Li, H., Smith, S.A., Di Toro, G., Suppe, J., Song, S.R., Nielsen, S., Sheu, H.S., Si, J., 2014. Gouge graphitization and dynamic fault weakening during the 2008 Mw 7.9 Wenchuan earthquake. Geology 42 (1), 47–50.

Kuo, L.W., di Felice, F., Spagnuolo, E., di Toro, G., Song, S.R., Aretusini, S., Li, H., Suppe, J., Si, J., Wen, C.Y., 2017. Fault gouge graphitization as evidence of past seismic slip. Geology 45 (1), 979–982. https://doi.org/10.1130/G39295.1.

Kuo, L.W., Huang, J.R., Fang, J.N., Si, J., Li, H., Song, S.R., 2018a. Carbonaceous materials in the fault zone of the longmenshan fault belt: 1. Signatures within the deep wenchuan earthquake fault zone and their implications. Minerals 8 (9), 385. https://doi.org/10.3390/min8090385.

Kuo, L.W., Huang, J.R., Fang, J.N., Si, J., Song, S.R., Li, H., Yeh, E.C., 2018b. Carbonaceous materials in the fault zone of the longmenshan fault belt: 2. Characterization of fault gouge from deep drilling and implications for fault maturity. Minerals 8 (9), 393. https://doi.org/10.3390/min8090393.

Lahfid, A., Beyssac, O., Deville, E., Negro, F., Chopin, C., Goffé, B., 2010. Evolution of the Raman spectrum of carbonaceous material in low-grade metasediments of the Glarus Alps (Switzerland). Terra Nova 22 (5), 354–360. https://doi.org/10.1111/j.1365-3121.2010.00956.x.

Lewan, M.D., 1983. Effects of thermal maturation on stable organic carbon isotopes as determined by hydrous pyrolysis of Woodford Shale. Geochim. Cosmochim. Acta 47 (8), 1471–1479. https://doi.org/10.1016/0016-7037(83)90306-X.

Li, K., Rimmer, S.M., Liu, Q., Zhang, Y., 2019. Micro-Raman spectroscopy of microscopically distinguishable components of naturally graphitized coals from Central Hunan Province, China. Energy Fuels 33 (2), 1037–1048. https://doi.org/10.1021/acs.energyfuels.8b04065.

Li, K., Rimmer, S.M., Presswood, S.M., Liu, Q., 2020. Raman spectroscopy of intruded coals from the Illinois Basin: Correlation with rank and estimated alteration temperature. Int. J. Coal Geol. 219, 103369 https://doi.org/10.1016/j.coal.2019.103369.

Lindgren, P., Parnell, J., 2006. Rapid heating of carbonaceous matter by igneous intrusions in carbon-rich shale, Isle of Skye, Scotland: an analogue for heating of carbon in impact craters? Int. J. Astrobiol. 5 (4), 343–351. https://doi.org/10.1017/S1473550406003442.

Liu, D.H., Xiao, X.M., Tian, H., Min, Y.S., Zhou, Q., Cheng, P., Shen, J.G., 2013. Sample maturation calculated using Raman spectroscopic parameters for solid organics:

methodology and geological applications. Chin. Sci. Bull. 58 (11), 1285–1298. https://doi.org/10.1007/s11434-012-5535-y.
Lünsdorf, N.K., 2016. Raman spectroscopy of dispersed vitrinite - methodical aspects and correlation with reflectance. Int. J. Coal Geol. 153, 75–86. https://doi.org/10.1016/j.coal.2015.11.010.
Lünsdorf, N.K., Dunkl, I., Schmidt, B.C., Rantitsch, G., von Eynatten, H., 2017. Towards a higher comparability of geothermometric data obtained by Raman spectroscopy of carbonaceous material. Part 2: a revised geothermometer. Geostand. Geoanal. Res. 41 (4), 593–612. https://doi.org/10.1111/ggr.12178.
Lünsdorf, N.K., Lünsdorf, J.O., 2016. Evaluating Raman spectra of carbonaceous matter by automated, iterative curve-fitting. Int. J. Coal Geol. 160, 51–62. https://doi.org/10.1016/j.coal.2016.04.008.
Luque, F.J., Ortega, L., Barrenechea, J.F., Millward, D., Beyssac, O., Huizenga, J.M., 2009. Deposition of highly crystalline graphite from moderate-temperature fluids. Geology 37 (3), 275–278. https://doi.org/10.1130/G25284A.1.
Luque, F., Rodas, M., 1999. Constraints on graphite crystallinity in some Spanish fluid-deposited occurrences from different geologic settings. Mineral. Deposita 34, 215–219. https://doi.org/10.1007/s001260050198.
Marshall, C.P., Edwards, H.G., Jehlicka, J., 2010. Understanding the application of Raman spectroscopy to the detection of traces of life. Astrobiology 10 (2), 229–243. https://doi.org/10.1089/ast.2009.0344.
Marynowski, L., Simoneit, B.R.T., 2009. Widespread upper triassic to lower jurassic wildfire records from poland: evidence from charcoal and pyrolytic polycyclic aromatic hydrocarbons. Palaios 24 (12), 785–798. https://doi.org/10.2110/palo.2009.p09-044r.
Maslova, O.A., Ammar, M.R., Guimbretière, G., Rouzaud, J.N., Simon, P., 2012. Determination of crystallite size in polished graphitized carbon by Raman spectroscopy. Phys. Rev. B 86 (13), 134205. https://doi.org/10.1103/PhysRevB.86.134205.
Mauquoy, D., Payne, R.J., Babeshko, K., Bartlett, R., Boomer, I., Bowey, H., Evans, C.D., Ring-Hrubesh, F., Muirhead, D., O'Callaghan, M., Piotrowska, N., Rush, G., Sloan, T., Smeaton, C., Tsyganov, A.N., Mazei, Y.A., 2020. Falkland Island peatland development processes and the pervasive presence of fire. Quat. Sci. Rev. 240, 106391 https://doi.org/10.1016/j.quascirev.2020.106391.
Mi, J., He, K., Fan, J., Hu, G., Zhang, B., 2019. Thermal maturity determination for oil prone organic matter based on the Raman spectra of artificial matured samples. Vib. Spectrosc. 104, 102940 https://doi.org/10.1016/j.vibspec.2019.102940.
Morga, R., 2011. Micro-Raman spectroscopy of carbonized semifusinite and fusinite. Int. J. Coal Geol. 87 (3-4), 253–267. https://doi.org/10.1016/j.coal.2011.06.016.
Mori, H., Mori, N., Wallis, S., Westaway, R., Annen, C., 2017. The importance of heating duration for Raman CM thermometry: evidence from contact metamorphism around the Great Whin Sill intrusion, UK. J. Metamorph. Geol. 35 (2), 165–180. https://doi.org/10.1111/jmg.12225.
Muirhead, D.K., Parnell, J., Taylor, C., Bowden, S.A., 2012. A kinetic model for the thermal evolution of sedimentary and meteoritic organic carbon using Raman spectroscopy. J. Anal. Appl. Pyrolysis 96, 153–161. https://doi.org/10.1016/j.jaap.2012.03.017.
Muirhead, D.K., Bond, C.E., Watkins, H., Butler, R.W.H., Schito, A., Crawford, Z., Marpino, A., 2020. Raman spectroscopy: an effective thermal marker in low temperature carbonaceous fold-thrust belts. Geol. Soc. Spec. Publ. 490 (1), 135–151. https://doi.org/10.1144/SP490-2019-27.
Muirhead, D.K., Bowden, S.A., Parnell, J., Schofield, N., 2017. Source rock maturation owing to igneous intrusion in rifted margin petroleum systems. J. Geol. Soc. 174 (6), 979–987. https://doi.org/10.1144/jgs2017-011.
Muirhead, D.K., Kedar, L., Schito, A., Corrado, S., Bond, C.E., Romano, C., 2021. Raman spectral shifts in naturally faulted rocks. Geochem. Geophys. Geosyst. 22 (10) https://doi.org/10.1029/2021GC009923 e2021GC009923.
Mukoyoshi, H., Kaneki, S., Hirono, T., 2018. Slip parameters on major thrusts at a convergent plate boundary: regional heterogeneity of potential slip distance at the shallow portion of the subducting plate. Earth Planets Space 70 (1), 1–10. https://doi.org/10.1186/s40623-018-0810-z.
Nakamura, Y., Oohashi, K., Toyoshima, T., Satish-Kumar, M., Akai, J., 2015. Strain-induced amorphization of graphite in fault zones of the Hidaka metamorphic belt, Hokkaido, Japan. J. Struct. Geol. 72, 142–161. https://doi.org/10.1016/j.jsg.2014.10.012.
Nakamura, Y., Yoshino, T., Satish-Kumar, M., 2017. An experimental kinetic study on the structural evolution of natural carbonaceous material to graphite. Am. Mineral. 102 (1), 135–148. https://doi.org/10.2138/am-2017-5733.
Nakamura, Y., Yoshino, T., Satish-Kumar, M., 2020. Pressure dependence of graphitization: implications for rapid recrystallization of carbonaceous material in a subduction zone. Contrib. Mineral. Petrol. 175 (4), 1–14. https://doi.org/10.1007/s00410-020-1667-2.
Negri, F., di Donato, E., Tommasini, M., Castiglioni, C., Zerbi, G., Müllen, K., 2004. Resonance Raman contribution to the D band of carbon materials: Modeling defects with quantum chemistry. J. Chem. Phys. 120 (24), 11889–11900. https://doi.org/10.1063/1.1710853.
Nemanich, R.J., Solin, S.A., 1979. First- and second-order Raman scattering from finite-size crystals of graphite. Phys. Rev. B 20 (2), 392. https://doi.org/10.1103/PhysRevB.20.392.
Nielsen, S.B., Clausen, O.R., McGregor, E., 2017. Basin% Ro: A vitrinite reflectance model derived from basin and laboratory data. Basin Res. 29, 515–536. https://doi.org/10.1111/bre.12160.
Paris, O., Zollfrank, C., Zickler, G.A., 2005. Decomposition and carbonisation of wood biopolymers - A microstructural study of softwood pyrolysis. Carbon 43 (1), 53–66. https://doi.org/10.1016/j.carbon.2004.08.034.
Parnell, J., Osinski, G.R., Lee, P., Green, P.F., Baron, M.J., 2005. Thermal alteration of organic matter in an impact crater and the duration of postimpact heating. Geology 33 (5), 373–376. https://doi.org/10.1130/G21204.1.
Parnell, J., Bowden, S.A., Muirhead, D., Blamey, N., Westall, F., Demets, R., Verchovsky, S., Brandstätter, F., Brack, A., 2011. Preservation of organic matter in the STONE 6 artificial meteorite experiment. Icarus 212 (1), 390–402. https://doi.org/10.1016/j.icarus.2010.11.029.
Pasteris, J.D., Wopenka, B., 1991. Raman spectra of graphite as indicators of degree of metamorphism. Can. Mineral. 29 (1), 1–9.
Pensa, A., Capra, L., Giordano, G., Corrado, S., 2018. Emplacement temperature estimation of the 2015 dome collapse of Volcán de Colima as key proxy for flow dynamics of confined and unconfined pyroclastic density currents. J. Volcanol. Geotherm. Res. 357, 321–338. https://doi.org/10.1016/j.jvolgeores.2018.05.010.
Pensa, A., Porreca, M., Corrado, S., Giordano, G., Cas, R., 2015. Calibrating the pTRM and charcoal reflectance (Ro%) methods to determine the emplacement temperature of ignimbrites: Fogo A sequence, São Miguel, Azores, Portugal, as a case study. Bull. Volcanol. 77 (3), 1–19. https://doi.org/10.1007/s00445-015-0904-4.
Pimenta, M.A., Dresselhaus, G., Dresselhaus, M.S., Cançado, L.G., Jorio, A., Saito, R., 2007. Studying disorder in graphite-based systems by Raman spectroscopy. Phys. Chem. Chem. Phys. 9 (11), 1276–1290. https://doi.org/10.1039/b613962k.
Pócsik, I., Hundhausen, M., Koós, M., Ley, L., 1998. Origin of the D peak in the Raman spectrum of microcrystalline graphite. J. Non-Cryst. Solids 227, 1083–1086. https://doi.org/10.1016/S0022-3093(98)00349-4.
Quirico, E., Rouzaud, J.N., Bonal, L., Montagnac, G., 2005. Maturation grade of coals as revealed by Raman spectroscopy: Progress and problems. Spectrochimica Acta Part A: Molecular and Biomolecular Spectroscopy 61 (10), 2368–2377. https://doi.org/10.1016/j.saa.2005.02.015.
Rabinowitz, H.S., Savage, H.M., Polissar, P.J., Rowe, C.D., Kirkpatrick, J.D., 2020. Earthquake slip surfaces identified by biomarker thermal maturity within the 2011 Tohoku-Oki earthquake fault zone. Nat. Commun. 11 (1), 1–9. https://doi.org/10.1038/s41467-020-14447-1.
Rebelo, S.L.H., Guedes, A., Szefczyk, M.E., Pereira, A.M., Araújo, J.P., Freire, C., 2016. Progress in the Raman spectra analysis of covalently functionalized multiwalled carbon nanotubes: Unraveling disorder in graphitic materials. Phys. Chem. Chem. Phys. 18 (18), 12784–12796. https://doi.org/10.1039/c5cp06519d.
Reich, S., Thomsen, C., 2004. Raman spectroscopy of graphite. Philos. Trans. R. Soc. A Math. Phys. Eng. Sci. 362 (1824), 2271–2288. https://doi.org/10.1098/rsta.2004.1454.
Ross, J., Bustin, R.M., 1990. The role of strain energy in creep graphitization of anthracite. Nature 343 (6253), 58–60. https://doi.org/10.1038/343058a0.
Ross, J., Bustin, R.M., Rouzaud, J.N., 1991. Graphitization of high rank coals-the role of shear strain: experimental considerations. Org. Geochem. 17 (5), 585–596. https://doi.org/10.1016/0146-6380(91)90002-2.
Rumble, D., 2014. Hydrothermal graphitic carbon. Elements 10 (6), 427–433. https://doi.org/10.2113/gselements.10.6.427.
Sadezky, A., Muckenhuber, H., Grothe, H., Niessner, R., Pöschl, U., 2005. Raman microspectroscopy of soot and related carbonaceous materials: Spectral analysis and structural information. Carbon 43 (8), 1731–1742. https://doi.org/10.1016/j.carbon.2005.02.018.
Sanders, M.M., Jubb, A.M., Hackley, P.C., Peters, K.E., 2022. Molecular mechanisms of solid bitumen and vitrinite reflectance suppression explored using hydrous pyrolysis of artificial source rock. Org. Geochem. 165, 104371 https://doi.org/10.1016/j.orggeochem.2022.104371.
Schito, A., Corrado, S., 2020. An automatic approach for characterization of the thermal maturity of dispersed organic matter Raman spectra at low diagenetic stages. Geol. Soc. Spec. Publ. 484 (1), 107–119. https://doi.org/10.1144/SP484.5.
Schito, A., Romano, C., Corrado, S., Grigo, D., Poe, B., 2017. Diagenetic thermal evolution of organic matter by Raman spectroscopy. Org. Geochem. 106, 57–67. https://doi.org/10.1016/j.orggeochem.2016.12.006.
Schito, A., Pensa, A., Romano, C., Corrado, S., Vona, A., Trolese, M., Morgavi, D., Giordano, G., 2022. Calibrating carbonization temperatures of wood fragments embedded within pyroclastic density currents through raman spectroscopy. Minerals 12 (2), 203. https://doi.org/10.3390/min12020203.
Scott, A.C., Glasspool, I.J., 2005. Charcoal reflectance as a proxy for the emplacement temperature of pyroclastic flow deposits. Geology 33 (7), 589–592. https://doi.org/10.1130/G21474.1.
Sheng, C., 2007. Char structure characterised by Raman spectroscopy and its correlations with combustion reactivity. Fuel 86 (15), 2316–2324. https://doi.org/10.1016/j.fuel.2007.01.029.
Sheppard, R.E., Polissar, P.J., Savage, H.M., 2015. Organic thermal maturity as a proxy for frictional fault heating: Experimental constraints on methylphenanthrene kinetics at earthquake timescales. Geochim. Cosmochim. Acta 151, 103–116. https://doi.org/10.1016/j.gca.2014.11.020.
Spötl, C., Houseknecht, W., D., Jaques, R.C., 1998. Kerogen maturation and incipient graphitization of hydrocarbon source rocks in the Arkoma Basin, Oklahoma and Arkansas: A combined petrographic and Raman spectrometric study. Org. Geochem. 28 (9-10), 535–542. https://doi.org/10.1016/S0146-6380(98)00021-7.
Suchy, V., Frey, M., Wolf, M., 1997. Vitrinite reflectance and shear-induced graphitization in orogenic belts: A case study from the Kandersteg area, Helvetic Alps, Switzerland. Int. J. Coal Geol. 34 (1-2), 1–20. https://doi.org/10.1016/S0166-5162(97)00018-9.
Surup, G.R., Nielsen, H.K., Heidelmann, M., Trubetskaya, A., 2019. Characterization and reactivity of charcoal from high temperature pyrolysis (800–1600 °C). Fuel 235, 1544–1554. https://doi.org/10.1016/j.fuel.2018.08.092.

Sweeney, J.J., Burnham, A.K., 1990. Evaluation of a simple model of vitrinite reflectance based on chemical kinetics. AAPG bulletin 74 (10), 1559–1570. https://doi.org/10.1306/0C9B251F-1710-11D7-8645000102C1865D.

Takahashi, K.U., Suzuki, N., 2017. Semi-open and closed system pyrolysis of Paleogene coal for evaluating the timing of hydrocarbon gas expulsion. Int. J. Coal Geol. 178, 100–109. https://doi.org/10.1016/j.coal.2017.05.004.

Theurer, T., Muirhead, D.K., Jolley, D., Mauquoy, D., 2021. The applicability of Raman spectroscopy in the assessment of palaeowildfire intensity. Palaeogeogr. Palaeoclimatol. Palaeoecol. 570, 110363 https://doi.org/10.1016/j.palaeo.2021.110363.

Theurer, T., Naszarkowski, N., Muirhead, D.K., Jolley, D., Mauquoy, D., 2022. Assessing modern calluna heathland fire temperatures using Raman spectroscopy: Implications for past regimes and geothermometry. Front. Earth Sci. 10, 82793. https://doi.org/10.3389/feart.2022.827933.

Tuinstra, F., Koenig, J.L., 1970. Raman spectrum of graphite. J. Chem. Phys. 53 (3), 1126–1130. https://doi.org/10.1063/1.1674108.

Urban, O., Jehlička, J., Pokorný, J., Rouzaud, J.N., 2003. Influence of laminar flow on preorientation of coal tar pitch structural units: Raman microspectroscopic study. Spectrochim. Acta Part A: Mol. Biomol. Spectrosc. 59 (10), 2331–2340. https://doi.org/10.1016/S1386-1425(03)00076-3.

Van Krevelen, D.W., Te Nijenhuis, K., 2009. Properties of Polymers: Their Correlation with Chemical Structure; Their Numerical Estimation and Prediction from Additive Group Contributions, fourth ed. Elsevier, Amsterdam, p. 1030. ISBN: 9780080548197.

Wang, D., 2012. Comparable study on the effect of errors and uncertainties of heat transfer models on quantitative evaluation of thermal alteration in contact metamorphic aureoles: Thermophysical parameters, intrusion mechanism, pore-water volatilization and mathematical equations. Int. J. Coal Geol. 95, 12–19. https://doi.org/10.1016/j.coal.2012.02.002.

Wang, D., Lu, X., Xu, S., Hu, W., 2008. Comment on "Influence of a basic intrusion on the vitrinite reflectance and chemistry of the Springfield (No. 5) coal, Harrisburg, Illinois" by Stewart et al. (2005). Int. J. Coal Geol. 73 (2), 196–199. https://doi.org/10.1016/j.coal.2007.03.004.

Wilkins, R.W.T., Boudou, R., Sherwood, N., Xiao, X., 2014. Thermal maturity evaluation from inertinites by Raman spectroscopy: The "RaMM" technique. Int. J. Coal Geol. 128, 143–152. https://doi.org/10.1016/j.coal.2014.03.006.

Wood, D.A., 2018. Kerogen conversion and thermal maturity modelling of petroleum generation: Integrated analysis applying relevant kerogen kinetics. Marine and Petroleum Geology 89, 313–329. https://doi.org/10.1016/j.marpetgeo.2017.10.003.

Wopenka, B., Pasteris, J.D., 1993. Structural characterization of kerogens to granulite-facies graphite: applicability of Raman microprobe spectroscopy. Am. Mineral. 78 (5-6), 533–557.

Yamauchi, S., Kurimoto, Y., 2003. Raman spectroscopic study on pyrolyzed wood and bark of Japanese cedar: Temperature dependence of Raman parameters. J. Wood Sci. 49 (3), 235–240. https://doi.org/10.1007/s10086-002-0462-1.

Yuan, L., Liu, Q., Mathews, J.P., Zhang, H., Wu, Y., 2021. Quantifying the structural transitions of chinese coal to coal-derived natural graphite by XRD, Raman spectroscopy, and HRTEM image analyses. Energy Fuel 35 (3), 2335–2346. https://doi.org/10.1021/acs.energyfuels.0c04019.

Zhang, S., Song, B., Cao, C., Zhang, H., Liu, Q., Li, K., Teppen, B.J., 2021. Structural evolution of high-rank coals during coalification and graphitization: x-ray diffraction, raman spectroscopy, high-resolution transmission electron microscopy, and reactive force field molecular dynamics simulation study. Energy Fuel 35 (3), 2087–2097. https://doi.org/10.1021/acs.energyfuels.0c03649.

Zhou, Q., Xiao, X., Pan, L., Tian, H., 2014. The relationship between micro-Raman spectral parameters and reflectance of solid bitumen. Int. J. Coal Geol. 121, 19–25. https://doi.org/10.1016/j.coal.2013.10.013.

Zickler, G.A., Smarsly, B., Gierlinger, N., Peterlik, H., Paris, O., 2006. A reconsideration of the relationship between the crystallite size La of carbons determined by X-ray diffraction and Raman spectroscopy. Carbon 44 (15), 3239–3246. https://doi.org/10.1016/j.carbon.2006.06.029.